

EXPERIMENTAL DETERMINATION OF KINEMATIC PARAMETERS
IN ASSEMBLED PARALLEL KINEMATIC MECHANISMS

By

BERNHARD JOKIEL, JR.

A DISSERTATION PRESENTED TO THE GRADUATE SCHOOL
OF THE UNIVERSITY OF FLORIDA IN PARTIAL FULFILLMENT
OF THE REQUIREMENTS FOR THE DEGREE OF
DOCTOR OF PHILOSOPHY

UNIVERSITY OF FLORIDA

1999

Copyright 1999

by

Bernhard Jokieli, Jr.

This work is dedicated to my parents Bernhard and Lois Jokiel. Over the seemingly endless years of schooling, their love, support and encouragement helped me get through the toughest of times. They gave me the strength and energy to keep going, and taught me to never lose sight of the big picture.

ACKNOWLEDGEMENTS

I would like to thank Dr. John Ziegert, Dr. Jiri Tlustý and Dr. Scott Smith for giving me the chance in 1994 to join the Machine Tool Research Center (MTRC) under the National Science Foundation Machine Tool Traineeship. If it were not for this great opportunity to grow under such learned professionals, I more than likely would not have pursued a Ph.D. much less a master's degree.

Dr. John Ziegert has been a wellspring of ideas, and a limitless source of personal and professional support through all of my endeavors at UF. It has been a real pleasure to work for him, and I sincerely look forward to possibilities of future ventures.

Lothar Bieg., Don Plymale, Dennis Clingan, Chip Steinhaus, Ken Hontz. and Jon Baldwin at Sandia National Laboratories have contributed greatly to my work for the last three years. To simply say "thank you" isn't enough.

I also would like to thank Jeff Freeman, Mark Flubacher and Robert Bridges at SMX corporation for their support and technical expertise.

My friends at the MTRC over the years have made a profound impact on me. I have learned so much from them about many things. I thank them so much for their help, laughs and friendship. It has been a wonderful five years.

TABLE OF CONTENTS

	<u>page</u>
ACKNOWLEDGEMENTS	iv
ABSTRACT	v
CHAPTERS	
1 INTRODUCTION	1
1.1 Modeling Mechanisms and Kinematic Parameters	1
1.2 Kinematic Parameters in Serial Link Mechanisms (SLM's)	2
1.3 Parallel Kinematic Mechanisms	6
1.4 Scope of Research	10
2 LITERATURE REVIEW	12
2.1 Review of Selected Works on Stewart Platform Analysis	12
2.2 Review of Selected Works on Stewart Platform Calibration	14
2.3 Review of Selected Works on Data-Fitting	17
3 SEQUENTIAL DETERMINATION TECHNIQUE	19
3.1 Coordinate Reference Frames	19
3.2 Locating the R Frame in the M Frame	22
3.3 Identifying the Joint Centers of Rotation	27
3.4 Locating the Spindle Nose	33
3.5 Determining Strut Lengths	36
4 UNCERTAINTY ANALYSIS	39
4.1 Strut Extension Error Budget	39
4.2 SMX 4000 Laser Tracker Error Budget	48
4.3 Propagated Uncertainty in Recovered Parameters	48
4.4 Propagated Uncertainty in Machine Positioning	64

5	EXPERIMENTAL RESULTS	68
5.1	Description of Equipment Used	68
5.2	Results: Joint Center Locations	75
5.3	Results: Determining the Initial Lengths	81
5.4	Results: Strut Extension Mapping	83
5.5	Results: Dynamic Renishaw Ball Bar Tests	88
6	CONCUSION AND FUTURE WORK	91
6.1	Conclusion	91
6.2	Future Work	94
APPENDICIES		
A	COORDINATE TRANSFORMATIONS	97
A.1	Homogeneous Coordinates	97
A.2	Homogeneous Coordinate Transformations	98
B	FITTING DATA TO BASIC GEOMETRIC OBJECTS	102
B.1	Least Squares Method	102
B.2	Calculating the Best-Fit Sphere	103
B.3	Calculating the Best-Fit Circle	104
B.4	Calculating the Best-Fit Plane	105
B.5	Calculating the Best-Fit Skew Circle	106
B.6	Calculating the Best-Fit Line	107
C	STEWART PLATFORM KINEMATICS	109
C.1	Instantaneous Kinematics	109
C.2	Tool Path Planning with Single Fixed-Length Strut	111
D	FIXTURE DESIGN DRAWINGS	113
BIBLIOGRAPHY		120
BIOGRAPHICAL SKETCH		123

Abstract of Dissertation Presented to the Graduate School
of the University of Florida in Partial Fulfillment of the
Requirement for the Degree of Doctor of Philosophy

EXPERIMENTAL DETERMINATION OF KINEMATIC PARAMETERS
IN ASSEMBLED PARALLEL KINEMATIC MECHANISMS

By

Bernhard Jokiel, Jr.

August 1999

Chairperson: Dr. John C. Ziegert
Major Department: Mechanical Engineering

Over the last decade, a new breed of multi-axis machine tools and robots based on parallel kinematic mechanisms (PKMs) have been developed and marketed worldwide. The success of these machines in the manufacturing sector will ultimately depend on their reliability, versatility and the accuracy with which they perform their tasks. Positional accuracy in these machines is controlled by accurate knowledge of the geometry (joint locations and distances between joint pairs) of the mechanism. Since these machines tend to be rather large, the kinematic parameters are difficult to determine when these machines are in their fully assembled state. Successful determination of the kinematic parameters in fully assembled PKMs up to this point has been done by global optimization methods. However, these method are time consuming to execute, typically require precision artifacts and involve calculating the difficult forward kinematic solution. In this study, a new method for determining the kinematic parameters of assembled PKMs is developed. In the

novel approach presented, each kinematic parameter is determined individually and independently from the others. The proposed method is subjected to two uncertainty analyses. The first analysis is to determine the effects of data quality and machine positional uncertainty on the calculated kinematic parameters. The second analysis is to determine the effects of the calculated parameters on the uncertainty of the position of the platform using a specific machine and measuring instrument combination. The sequential determination technique was executed and the results implemented on a machine in the field. Results for Renishaw ball bar circles before and after calibration are presented.

CHAPTER 1 INTRODUCTION

The purpose of this chapter is twofold: first, to give the reader a broad-brush overview of modeling serial link mechanisms (SLMs) and parallel kinematic mechanisms (PKMs), and second to explain the importance of accurate kinematic parameters of a mechanism. This brief discussion of kinematic parameters and modeling is necessary to clarify the direction and importance of the statement of work and scope of the research discussed in the last part of this chapter.

1.1 Modeling Mechanisms and Kinematic Parameters

All machine tool and robot controllers are model-based, meaning the controller uses a mathematical relation to turn motions occurring at the joint axes of a mechanism into the resulting motion at the tool tip. In order for the controller to correctly position the tool tip, it must have an accurate kinematic model of the mechanism's structure. A kinematic model mathematically describes how the individual motions of interconnected components in a mechanism contribute to the overall motion of the tool point. An accurate kinematic model for a particular mechanism will provide accurate solutions for tool tip position, orientation, velocity and acceleration only if the values of the kinematic parameters upon which the model is based are an accurate reflection of the critical physical attributes of the system being controlled. Kinematic parameters are the dimensions of the mechanism's components which directly govern the mechanism's positioning accuracy.

From the standpoint of positioning accuracy it is extremely important that the model of the mechanism being used inside the machine controller exactly matches the mechanism it is directed to control.

1.2 Kinematic Parameters in Serial Link Mechanisms (SLMs)

SLM mechanisms are by far the most widely used and time proven geometries for most robots and machine tools. A SLM has a number of one degree of freedom (DOF) actuators “stacked” on top of one another in a chain such that one joint axis carries the second, which carries the third and so on until the desired number of actuators equals the needed DOF of motion. Thus a six-DOF mechanism requires six independently controllable joint axes. Each joint axis in the serial chain is responsible for a single motion relative to the links stacked above it.

1.2.1 SLM Robots

SLM robots are used in a number of repetitive tasks such as materials handling, assembly, welding, deburring and painting, particularly in the automotive industry. SLM robots are typically made from a series of links connected together end to end by revolute joints to form a highly dextrous, reconfigurable linkage much resembling the human arm (Figure 1.1). At the end of the link chain is a tool flange. Different types and configurations of tools may be connected to the tool flange to customize the robot for the particular task it is required to perform. The desired path for the robot to follow is programmed. Mathematical routines inside the controller convert the desired tool path into the appropriate motion of each of the revolute joints.

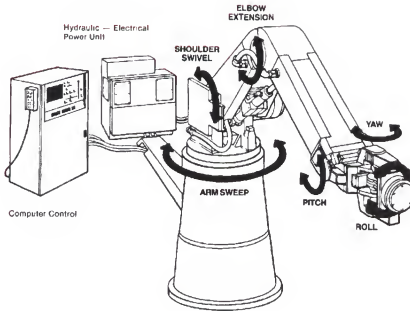


Figure 1.1 Construction of a typical SLM robot [1].

The accuracy with which the tool point may be positioned is directly dependent upon accurate knowledge of the location and orientation of each of the joints in the serial chain. This involves not only knowing precisely the motion occurring between the links at each joint, but also the exact dimensions between each of the joints up the serial chain. The link lengths, twist angles, offset distances and rotation at each joint are these critical dimensions and constitute the kinematic parameters for serial chain mechanisms. Figure 1-2 depicts a single link with two revolute joints. Knowing the kinematic parameters for each link, coordinate transformations may be created which express the position and orientation of link $i+1$ relative to link i . By multiplying together the transformations between each link, the position of the tool center point of the end effector may be determined relative to the work frame.

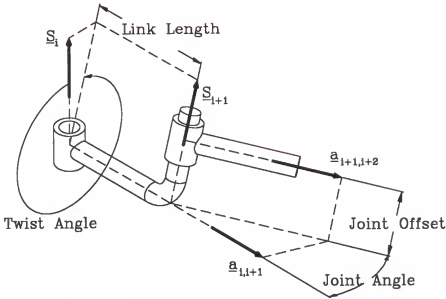


Figure 1.2 Kinematic parameters of a serial arm link.

1.2.2 SLM Milling Machines

Since most milled parts are rectangular in nature based on a Cartesian reference frame, it is convenient to construct these machines with three mutually perpendicular, straight linear guideways, one for each linear motion along the Cartesian X,Y and Z axes (Figure 1.3). Rotary tables which provide rotation about axes parallel to the X, Y, and/or Z axes may be used to rotate the spindle, the workpiece or both to achieve motion in five or more DOF.

By knowing precisely the direction and the amount of movement of each of the carriages translating along the guideways, the position of the tool tip relative to the workpiece can be accurately determined. The accuracy with which this linear motion is achieved is dependent directly upon the straightness and parallelism of the guideways and their degree of mutual perpendicularity. Variations in the straightness and parallelism of the guideways

may be mapped through precise measurements to yield the classic six error motion profiles for small translational and rotational motions for each guideway (Figure 1.4).

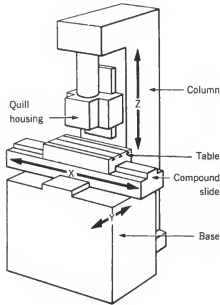


Figure 1.3 Schematic of three-axis stacked-slide SLM machine tool [2].

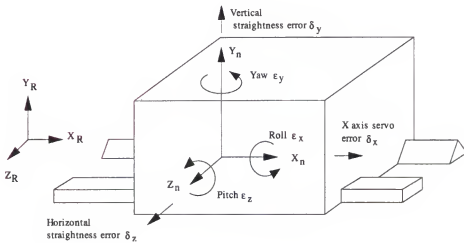


Figure 1.4 Error motions in a single linear guideway [3].

For a three-axis machine tool, there are 18 functional error motion relations plus three mutual perpendicularity parameters for a total of 21 relations. This set of relations constitutes the kinematic parameters for a three-axis milling machine.

1.3 Parallel Kinematic Mechanisms

PKM devices are a relatively new field in robot and machine tool technology. Several companies and many universities world wide have invested a great deal of time, effort and money researching this new area of mechanism technology. The main distinction between PKM and SLM devices is the way the actuators connect the machine reference frame to the moving frames. As explained in previous section, the mechanical links and actuators of a SLM device are connected end to end to form a chain from the reference frame to the tool tip. In PKM devices, one end of each actuator is connected to the reference frame while the other is connected to the moving frame to be controlled.

1.3.1 Parallel Platform PKMs

One example of a PKM configuration is the Stewart platform. This configuration involves six linear actuators. Each actuator (or strut) is connected between a fixed base frame and a moving platform by spherical joints at either end. By extending and retracting the extensible links, the position and orientation of the platform can be affected, yielding motion in all six-DOF (Figure 1.5). From Figure 1.5 it can be seen that the pose of the platform is controlled only by the joint locations and the strut lengths. In order to accurately control the location and orientation of the tool held in the spindle, it is necessary to accurately know the locations of all of the joints, the pose of the spindle relative to the platform joints, and the strut lengths between the base and platform joint pairs.

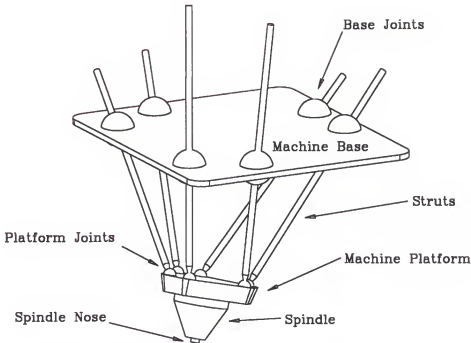


Figure 1.5 A 12-joint (6-6) Stewart platform six-DOF device.

1.3.2 Spatial Location of Joint Centers of Rotation

Each spherical joint has a Cartesian (X,Y,Z) location in space, therefore each joint has 3 parameters to define its location. Parallel platform PKMs which have 12 joints (six on the base frame and six on the platform or 6-6) have 42 kinematic parameters (for ball and socket joints), 36 for the joint locations and six for the distances between connected joint pairs. Others which have nine joints (six on the base and three on the platform or 6-3) have 33 kinematic parameters, 27 for the joint locations and six for the distances between connected joint pairs.

1.3.3 Spindle Nose Location and Orientation

In order to properly move the tip of a tool in a spindle attached to the platform to the correct desired position, it is necessary to know exactly where the spindle nose is located

and how it is oriented with respect to the platform joint centers. Once the correct location and orientation are known, the correct coordinate transformations can be calculated to properly guide the tool tip. The spindle nose location and orientation account for five additional kinematic parameters.

1.3.4 Initial Strut Reference Lengths

When a PKM device is first switched on, the machine's controller has no information regarding the extension state of each strut. The first task the controller performs is to bring the platform to its home position. This typically involves fully retracting the struts to their limit switches, followed by an encoder index pulse servo search. Once all of the encoders are at their index marks, the machine assigns to each strut an initial strut reference length. The value assigned to each homed strut is supposed to be the exact distance between the base joint centers and their paired platform centers at home position. The initial length provides a reference to which length commands will be added and subtracted in order to control the motion of the platform. Since the total distance between paired joint centers at any time is directly dependent upon accurate knowledge of the initial reference length, the initial reference lengths become critical components of the total strut length (Figure 1.6).

1.3.5 Strut Length Extension Error

The purpose of leadscrew error compensation is to correct the distance traveled along the leadscrew for small deviations in the pitch of the screw which drives the axis. For this feature to work properly, an accurate map of the deviations of the pitch of each leadscrew in the system is required (Figure 1.7).

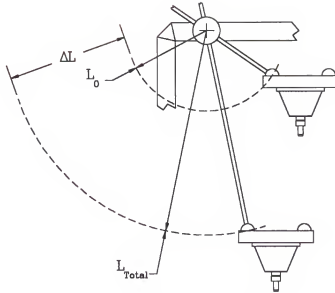


Figure 1.6 Relation between home length and total strut length.

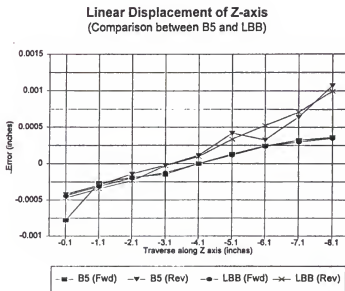


Figure 1.7 Typical map of leadscrew pitch variation “B5” refers to the ASME B5.54 standard, “LBB” refers to Laser Ball Bar [4].

Based on the controller’s calculated position along the screw, the controller will add or subtract a small amount from the commanded position based on these screw pitch error

maps. Screw pitch error maps by themselves do not constitute new kinematic parameters, but the potential enhancement in positional accuracy for PKM mechanisms makes creating such maps a worthwhile endeavor.

1.4 Scope of Research

The research discussed herein has three individual goals. The first goal is to create a new PKM calibration method which can be used on fully assembled PKM machines in the field to identify all of the kinematic parameters of a particular machine. The second is to perform an uncertainty analysis on the recovered kinematic parameters to determine the feasibility of calibration and the effect of uncertainties in the recovered kinematic parameters with their uncertainties on the positional accuracy of the milling machine. The third is to implement the new method on a PKM device in the field and verify the success of the method.

1.4.1 Develop PKM Calibration Method

The calibration scheme to be developed must meet three basic requirements. First, all of the kinematic parameters (joint center locations, initial strut lengths, spindle position and orientation) and screw pitch error maps for the given machine must be determined with the machine fully assembled. The machine should not be disassembled to determine any of the kinematic parameters, nor should any machine component require a second external measurement process (like a CMM inspection) to recover any of the kinematic parameters. Second, the calibration scheme should not rely on precision artifacts which are specially designed, fabricated and maintained for the single purpose of calibration. Third, the technique should take a relatively short time to execute (2-3 business days).

1.4.2 Uncertainty Analysis

All measurements have some uncertainty associated with them. Uncertainty is a reflection of the quality and reliability of the measurement. It is important when reporting experimental results to perform an uncertainty analysis and report the amount of uncertainty in the measurement or in a parameter derived from experimental measurements. In this research it is important to not only report the uncertainty in the recovered kinematic parameters, but also to show the propagated uncertainty at the tool tip when the recovered kinematic parameters are implemented in the controller.

1.4.3 Verification of Method

The final step in this research is to perform the complete calibration scheme and uncertainty analysis on a PKM in the field. The machine chosen is a Hexel Tornado 2000 milling machine installed at Sandia National Laboratories in Albuquerque, New Mexico. The kinematic parameters for the particular machine will be recovered, an uncertainty analysis will be performed, and verification tests performed to validate the method.

CHAPTER 2 LITERATURE REVIEW

A large body of work exists covering all aspects of parallel mechanisms. The purpose of this chapter is to sample the existing literature and review selected works which appear to be directly applicable to the scope of the research presented in Chapter 1. The bibliography at the end of this work contains a larger list of papers which were read, but not presented in this chapter. Three main areas are reviewed in this chapter - analysis of Stewart Platform mechanisms, existing calibration schemes for parallel mechanisms, and fitting of surfaces to data points.

2.1 Review of Selected Works on Stewart Platform Analysis

The “Stewart platform” was first proposed by D. Stewart in 1965 in a paper entitled “A Platform with Six Degrees of Freedom” [5]. In this paper, Stewart proposes several ideas for a moving platform controlled in six degrees of freedom (three translational, three rotational) relative to a stationary frame. He describes in detail a three-strut and a six-strut design where the struts work in parallel with each other to control the motion of the platform. In the three-strut design, the struts are extensible and servo controlled. They are attached to the ground frame by two-DOF gimbal joints where one rotary joint is servo controlled while the other is passive. The struts are attached to the platform by passive three-DOF ball and socket joints. The second design is similar to the first, but utilizes six servo controlled struts connected in pairs to the platform. All of the joints connecting the

struts to the ground and platform are passive. Three of the legs are connected to the platform, the other struts are connected to the ground-platform legs at their mid points. In this manner, control of the platform is achieved by extending and retracting the legs without active control of the rotary joints. Analysis of the working volumes of such mechanisms, and rules of thumb for design are also discussed. The second half of the paper is a peer comment section where other researchers working in this area comment on Stewart's work. It is in this section that the typical six legged design is shown where each leg is connected between the ground and the platform. It is also in this section where the ideas of using these mechanisms in the design of machine tools, flight simulators, and isolation pads on ships are developed. Although this paper does not discuss calibration of parallel platforms, it is the first paper to focus attention on the development of a new methodology for design of machine tools and robots.

A unique, completely algebraic closed-form solution for the forward kinematics of a symmetric 6-3 parallel platform (a six extensible strut mechanism, with six base joints and three platform joints) is rigorously derived in a paper entitled "Kinematic Analysis of a Stewart Platform Manipulator" by Liu, Fitzgerald and Lewis [6]. The calculation of the poses for several special cases are discussed as well such as the lowest, highest, most tilted and most twisted platform poses. In the work to be proposed in Chapter 3, the forward kinematic solution is not required, but this paper did provide the correct rotation matrix between the base and platform frames for rotations about the X, Y and Z axes. The forward analysis proposed of the 6-3 platform is useful, but it is not a general solution for any 6-3 or 6-6 configuration of base and platform joints.

The paper entitled “Vibration Analysis of Stewart-Platforms” by Yang and Masory [7] provides a very concise and useful analysis of the stiffness and vibration mode shapes for general 6-6 Stewart platforms. A quick overview of the construction of the Jacobian, static force analysis, and sensitivity to small strut length deviations are covered which provides enough material for other researchers to do some very interesting work. Most of the paper is dedicated to modal vibration analysis, including the derivation of the stiffness matrix of the structure, the modal stiffness and mass matrices, and the vibrational mode shapes and frequencies for the system.

The two part paper by Wang and Masory [8] entitled “On the Accuracy of a Stewart Platform” discusses the importance and effects of positional errors of Stewart platform manipulators due to component manufacturing tolerances. In Part I, particular attention is paid to the development of an error model for the strut subassemblies consisting of two gimbal joints and a straight extensible member. However only the error model for gimbal joints is discussed, not ball joints. Strut lengths including estimated length errors are calculated and used by a numerical forward position solution algorithm to determine the position and orientation of the platform. The conclusion reached draws into question the hypothesis that Stewart platform mechanisms are inherently more accurate than serial manipulators. A common claim among researches is that parallel mechanism must be inherently more accurate than serial mechanisms since the inaccuracies in the joint locations and strut extensions occur are not additive. The conclusion reached in this work is that parallel mechanisms are at best on the same level of accuracy as serial mechanisms given similar amount of uncertainty in their joint locations. A $1/4$ ” error in position of a joint is claimed to cause up to a 1” position error of the tool tip.

2.2 Review of Selected Works on Stewart Platform Calibration

Part II of the paper “On the Accuracy of a Stewart Platform” by Masory et al [9], presents a numerical global calibration scheme using a small number of poses to determine 42 kinematic parameters based upon an error-model approach. The method requires measurements of the platform pose (location and orientation), the corresponding strut lengths, and initial guesses of the parameters. The method then proceeds to iterate through the poses to develop new guesses of the parameters. These new guesses are used to formulate a third set of parameters. This process continues until the pose error norm has converged to zero. One of the drawbacks of such a method is the numerical calculation of the Jacobian at each pose, which proves to be a very time consuming endeavor. Each iteration through the minimization requires 11 hours on a Sun workstation model 3/260. Since it takes at least four iterations to achieve the desired results, it takes a minimum of 44 hours to calibrate the machine after the input data is collected (data collection time not given). Using simulated data with a random noise component within ± 0.0024 the parameters were estimated to be within ± 0.025 from their nominally perfect values.

Tajbakhsh and Ferreira’s paper “Kinematic Error Estimation and Transmission Error Bounding for Stewart Platform Based Machine Tools” [10] covers two areas: experimentally determining the kinematics parameters of a Stewart platform, and determining the bound for the positional error due to the errors in strut length and joint sphericity. For general 6-6 mechanisms, a global calibration method is proposed for determining the kinematic parameters. Vector expressions for the length of each strut are derived and expanded to reveal all 42 kinematic parameters. An objective function is created from the strut lengths which is to be minimized using least squares over a series of observations. The

input data into the minimization algorithm is the measured change in the strut lengths resulting from probing a known artifact such as a ball plate. The simulation results are encouraging in that they accurately reflect the amount of error present in the simulated kinematic parameters. However these simulations do not include measurement noise or uncertainty.

In Zhuang and Roth's publication "Method for Kinematic Calibration of Stewart Platforms" [11], they propose to hold each strut at a fixed length in turn over a set of poses. At each pose, the length of each strut and the platform pose is measured. The strut length is measured through some sort of length transducer, but it is not clear how they propose to measure to platform orientation and location. The input data is used as in the previous two methods, in a global optimization scheme through continuous recalculation of the Jacobian. In simulation utilizing measurement noise levels of 0.02mm and 18 poses the estimated error in the position of the platform was as much as 3mm. No experimental verification was presented.

Zhuang, Liu and Masory's paper "Autonomous Calibration of Hexapod Machine Tools" [12] presents a method for calibrating a Stewart platform mechanism using no external measurements. Instead, measurement of joints angles and strut lengths are made by many redundant sensors attached to the joints and struts. At specific locations along a predetermined path, all of the sensors are read capturing a complete picture of the structure of the machine. This data is then used in a global optimization scheme which is very similar in nature to the others discussed in this literature review, by using an optimization technique on an error model. In simulation, the expected error in position after the calibration of the simulated machine was 0.005" without signal noise. Experimental results are

included claiming a 52% reduction in position error. One of the shortcomings of the method pointed out in the paper was the fact the spindle could not be included in the calibration. Once the locations of the platform joints are known, the spindle orientation and location must be determined by a second process.

2.3 Review of Selected Works on Data-Fitting

A paper by Bourdet, Lartigue, and Leveaux entitled “Effects of Data Point Distribution and Mathematical Model on Finding the Best-Fit Sphere to Data” [13] proposes two least squares approaches for fitting CMM data to the equation of a sphere. Two algorithms are proposed, one which fits input data to four parameters (x_c, y_c, z_c, r_c) and another which assumes r_c to be known. The proposed algorithms are rigorously tested for 5, 9 and 13 data point patterns over cone angles ranging from 10° to 110° . Simulated results show that for cone angles below 30° , the accuracy of the estimate of the location of the sphere center worsens quickly with the decrease in cone angle. Input data is assumed corrupted along the radius of the sphere by $1\mu\text{m}$ maximum. The pattern of the data point locations is symmetrical in each case. A random dispersion of points over the surface is not considered in this work.

The last paper to be reviewed is by Baldwin, Henke, Casou and Brown entitled “Optimizing Discrete Point Sample Patterns and Measurement Data Analysis on Internal Cylindrical Surfaces with Systematic Form Deviation” [14]. In this work, the object was to determine the optimal number and location of data points which best measure an internal cylindrical surface for a given manufacturing process. In this process, a number of holes were made in aluminum plates by various methods (milling, drilling, reaming and boring).

Each of the holes were densely measured by a scanning probe on a very precise CMM. The frequency content of the data points (eigen-surfaces) to the best fit surface was analyzed. Based upon the frequency content, the optimal location and number of data points to be measured is then deduced by an optimization scheme. Although this process was specifically designed for cylinders, it is claimed in the paper that in fact the same process can be used for any object of any shape. Optimal locations of data collection points is not included in the scope of the research to be undertaken in this work.

CHAPTER 3

SEQUENTIAL DETERMINATION TECHNIQUE

The material in this chapter covers a novel generalized technique for recovering the kinematic parameters of a fully assembled Stewart platform milling machine or robotic manipulator. The technique described in this chapter is intended to be used with some sort of a spatial coordinate measuring device such as a portable articulated CMM measuring arm (Romer, Faro, etc.), a Laser Ball Bar (LBB), or a laser tracker (SMX, API, etc). The material to be presented is as follows: (1) introduction to the coordinate reference frames used; (2) locating the reference frame relative to the machine frame; (3) identification of the joint center locations; (4) identification of the spindle nose position and orientation relative to the platform joints; (5) recovery of the initial strut lengths; and (6) mapping of strut length errors.

3.1 Coordinate Reference Frames

Several different coordinate reference frames are required during the calibration execution. Some of these frames are solely used by the milling machine's controller, while others are strictly used as measurement reference frames during the calibration cycle (Figure 3.1). This section briefly describes each frame's location and purpose for the Hexel Tornado 2000 milling machine.

3.1.1 Machine Coordinate Reference Frames

3.1.1.1 Machine frame (M)

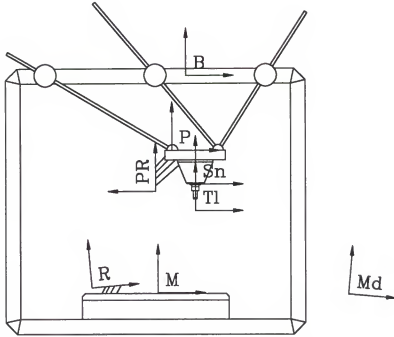


Figure 3.1 Coordinate reference frame locations on a planar Stewart platform device.

The M frame is the reference frame for all machine motion where $(0,0,0)$ is the origin of the machine. Motions to be executed in part programs must ultimately be transformed into this system in order to be properly interpreted by the controller.

3.1.1.2 Tool frame (Tl)

The origin of the Tl system is located at the tool tip. The Z-axis unit vector is always colinear with the tool/spindle axis. The X-axis is initially parallel to the X-axis of the M system, but may be commanded to rotate about the X, Y, or Z axes of the M system. The orientation and position of this system relative to the M system is controlled by part motion programs.

3.1.1.3 Spindle nose frame (Sn)

The Sn system is parallel with the T1 system, but is translated along the Z-axis (tool centerline) of the T1 system to the spindle nose by the tool length.

3.1.1.4 Platform joint frame (P)

The P frame is controlled by the position of the platform joints. Its origin lies at the center of the best fit circle created by the platform joint centers. Its Z-axis is parallel to the normal vector of the best fit plane created by the platform joint centers. Its X-axis is parallel to the unit vector running from joint five to joint two.

3.1.1.5 Base frame (B)

Similar to the P frame, the B frame is defined by the locations of the base joints. Its origin lies at the center of the best fit circle created by the base joint centers. The Z-axis is parallel to the normal vector of the best fit plane created by the base joint centers. The X-axis is parallel to the unit vector from joint five to joint two.

3.1.2 Measurement Coordinate Reference Frames

3.1.2.1 Measuring device frame (Md)

The Md frame is the reference frame inherent to the measuring device used. It is a floating reference frame whose location and orientation is variable relative to the R system, but fixed during a measurement cycle.

3.1.2.2 Central reference frame (R)

The R frame is extremely important to the calibration technique. This frame provides the single reference to which all of the spatial coordinate data collected in different Md

frames will be transformed. This frame is located on the top of the worktable. A method to determine the transformation between the R and M frames will be discussed in detail later in this chapter.

3.1.2.3 Platform reference frame (PR)

The PR frame is a local reference frame used to track motions of the platform relative to the Md and R systems, and is used to unify the measured coordinate data collected in the in the Sn and P frames. It has no specific location or orientation relative to the moving platform body itself. However, the PR frame's location and orientation once chosen stays constant relative to the platform body throughout the calibration process.

3.1.3 Homogeneous Coordinate Transformation Matrices

Homogenous coordinate transformation matrices (HTMs) are used to express coordinates measured in one coordinate reference frame in a second reference frame. Specifics on HTMs will not be presented here, but appear in Appendix A for readers who would like to familiarize themselves with the labelling convention, construction or implementation of HTMs.

3.2 Locating the R Frame in the M Frame

The first step in the calibration process is to determine the relationship between the R and M systems. Since PKM devices have no guideways to physically embody Cartesian motions, there is a great deal of flexibility in defining the location of the M system. Normally, a milling machine's worktable provides some kind of a reference for machine axis travels. T-slots in the worktable are typically aligned with the X-axis travel of the machine

(Figure 3.2). A convenient convention for the placement of the M system is to place the origin at the center of the worktable with the Z-axis parallel to the normal vector of the table (+Z up), and the X-axis parallel to the T-slots (+X to the right from the front of the machine).

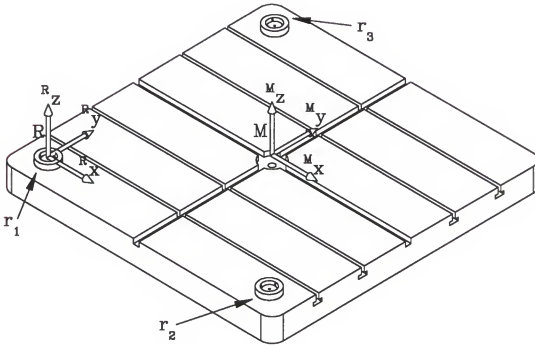


Figure 3.2 Location of machine reference (M) and central reference (R) frames.

3.2.1 Locating Frame R relative to the Md

Three gage points (labelled r_1 , r_2 , and r_3) used for the measurement device (usually some form of a kinematic mount) are secured at the farthest corners of the worktable. Mounts r_1 and r_2 are aligned approximately in the machine X direction. Mount r_3 is placed such that the line formed by r_1 and r_3 is approximately perpendicular to the line formed by r_1 and r_2 (Figure 3.2). Using proper procedures for the measurement device being used, the coordinates of each of the R gage points are measured relative to the Md system

several times. Using the mean coordinate values for each target mount location measured in the M_d system ($^{M_d}r_1$, $^{M_d}r_2$, $^{M_d}r_3$), the transformation $^{M_d}T_R$ (Appendix A) is constructed.

3.2.2 Frame M in the M_d

3.2.2.1 Determine the Z-axis unit vector

The coordinates of 30-40 uniformly distributed points on the flat surface of the table (not in the T-slots or on table surface blemishes) are measured relative to M_d (Figure 3.3). The coordinate locations are fit to the equation of a plane by the zero eigenvalue method (Appendix B). The calculated surface normal of the best-fit plane is the Z-axis unit vector of the M system expressed in, $^{M_d}z_M$.

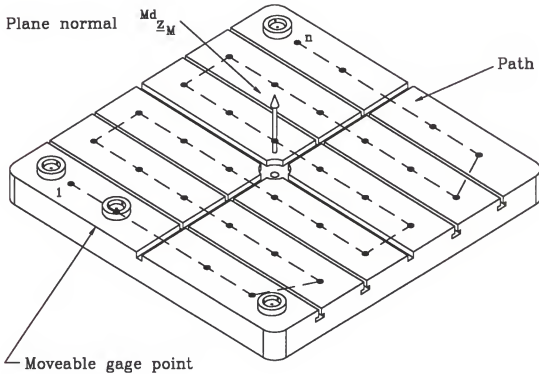


Figure 3.3 Location of sample points for table plane with surface normal $^{M_d}z_M$.

3.2.2.2 Determine the X-axis unit vector

Using fixture to ride in a T-slot as a straightedge, the coordinates of 10-20 points along a T-slot are measured relative to the M_d (Figure 3.4). These coordinates are fit to the equation of a line in three-space (Appendix B). The resulting unit vector of this best-fit line is projected into the best-fit plane. The part of the vector in the plane after unitization is the X-axis direction vector of the M system expressed in M_d , ${}^{M_d}\underline{\hat{x}}_M$.

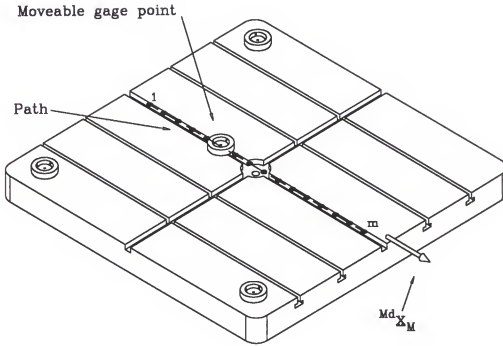


Figure 3.4 Location of machine x-axis sample points with direction vector ${}^{M_d}\underline{\hat{x}}_M$

3.2.2.3 Determine the Y-axis unit vector

The cross product of the Z and X-axis unit vectors is performed to determine the Y-axis unit vector of the M system expressed in M_d , ${}^{M_d}\underline{\hat{y}}_M$.

3.2.2.4 Determine the origin of the M frame

A desired location on the table is selected to be the machine's origin. The location of this point is measured relative to the Md system. The coordinates of this point are projected into the best-fit plane. The location of the projected point in the plane is the origin of the M system (Figure 3.5)

3.2.2.5 Calculate the HTM for M relative to Md

All of the information necessary to calculate the transformation ${}^M T_{Md}$ has now been experimentally determined, and may be assembled:

$${}^M T_{Md} = \begin{bmatrix} {}^{Md}x_M & {}^{Md}y_M & {}^{Md}z_M & {}^{Md}O_M \\ 0 & 0 & 0 & 1 \end{bmatrix}^{-1}$$

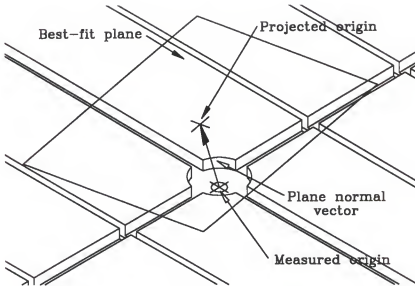


Figure 3.5 Location of the measured and projected M origin.

3.2.3 Calculate the HTM for M Relative to R

The transformation relating the R system to the M system, ${}^M T_R$, can now be calculated from the previously determined transformations ${}^M T_{Md}$ and ${}^{Md} T_R$.

$${}^M T_R = {}^M T_{Md} {}^{Md} T_R$$

3.3 Identifying the Joint Centers of Rotation

Determining the spatial coordinates of the spherical joints is conceptually very simple. The platform is moved along an arbitrary predetermined path while holding each strut in turn at an arbitrary fixed length (Appendix C). As the platform moves, the fixed-length strut rotates in its joints. Since this is a pure rotation, all of the points on the strut trace paths on concentric spherical shells relative to the strut's joint centers (assuming that the joints produce spherical motion and there is little strut bending) (Figure 3.6). In this manner, a gage point affixed to the strut will also rotate about the strut's joint centers. By measuring the strut gage point coordinates lying on its spherical shell at specific locations, and fitting these coordinates to the equation of a sphere, the locations of the base and platform joint centers can be calculated. Performing this method once for each of the six struts, the coordinates for all 12 of the base and platform joint centers may be recovered.

3.3.1 Strut Fixture

The configuration and construction of the strut fixture which holds the two targets SA and SB naturally must be tailored for the specific machine to be calibrated, but it in no way must be a precisely constructed piece of hardware (Figure 3.7a, Figure 3.7b)

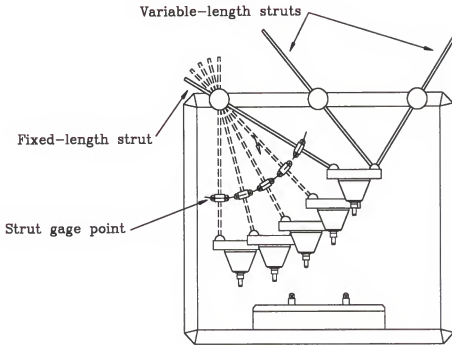


Figure 3.6 Strut fixture installed at the midpoint of a strut.



(a)



(b)

Figure 3.7 (a) Strut fixture close-up; (b) Strut fixture installed on Hexel Tornado 2000.

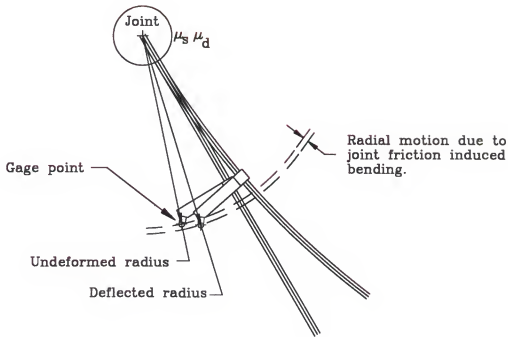
It is necessary to have two targets rather than a single target. If a strut were to bend during data collection, a target attached to the strut would translate radially, relative to the strut (Figure 3.8a) causing an apparent nonspherical joint motion. By situating the two targets (SA and SB) along a line, equidistant from the center of the strut, their coordinates may be averaged to calculate the coordinates of a point (SM) on the neutral axis of the strut where the effects of strut bending are negligible (Figure 3.8b).

3.3.2 Platform Fixtures

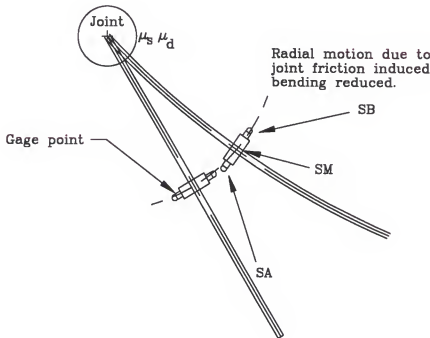
The success of this method depends on measuring a moving coordinate system PR attached to the platform. The PR system will be used to transform all relevant measurements into a single system which stays fixed relative to the platform. Therefore it is essential that the fixtures holding the targets on the platform are very secure, and are not moved during the entire measurement process. An example of a set of platform fixtures designed to clamp to the spindle housing of a Hexel Tornado 2000 milling machine is shown in Figure 3.9. When designing the fixtures and setting up for the measurement cycle, it is important to keep in mind that all of the targets (r_1 , r_2 , r_3 , SA, SB, pr_1 , pr_2 , and pr_3) must be visible to the chosen measuring instrument at all times for all motion paths.

3.3.3 Data Collection

It is important to check the setup to make sure that all of the gage points are visible to the chosen measuring device during the entire motion sequence for each strut. The location of the measuring apparatus' origin must not be moved during the data collection for the strut in question. It may be moved after the measurement process for the strut in question is complete to a more suitable location for the data collection for the next strut.



(a)



(b)

Figure 3.8 Strut fixture with (a) single gage point; (b) two gage points.

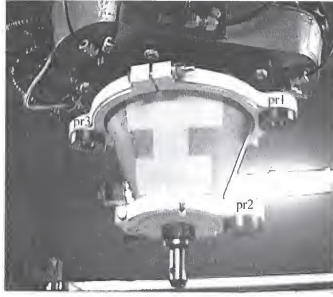


Figure 3.9 PR platform clamp fixtures installed on spindle.

3.3.3.1 Before motion program execution

Before the motion program for the j^{th} strut is executed, the location of the R system relative to the Md system must be acquired. This is done by measuring the coordinates of the three R gage points relative to the Md system, and calculating the HTM $(^{Md}T_R)_j$ (Appendix A).

3.3.3.2 During motion program execution

At the i^{th} specified location, the motion program for the j^{th} strut is stopped, at which time the spatial coordinates of the gage points SA, SB, pr₁, pr₂, and pr₃ are collected relative to the Md system, and then expressed in the M system. The mean of the $(^M\text{SA})_{j,i}$, and $(^M\text{SB})_{j,i}$ coordinates are calculated to produce $(^M\text{SM})_{j,i}$. The corresponding transformation $(^{Md}T_{PR})_{j,i}$ must also be calculated for the i^{th} pose from the PR gage point coordinates.

3.3.4 Recovery of the Base Joint Center Locations

The coordinates (${}^M\text{SM}$)_j are fit to the equation of a sphere using the method of least squares (Appendix B). Assuming perfect spherical motion, the center of the best fit sphere is coincident with the j^{th} strut base joint center. Hence the coordinates of the location of the j^{th} strut base joint center (${}^M\text{B}$)_j are the coordinates of the best-fit sphere center (revisit Figure 3.6).

3.3.5 Recovery of the Platform Joint Center Locations

To an observer stationary relative to the M system, a point on the fixed-length strut rotates about the base joint center. To an observer stationary relative to the P system, the same point appears to rotate about the strut's platform joint center.

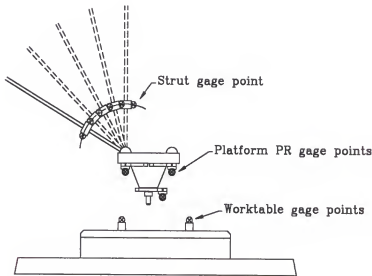


Figure 3.10 PR platform clamp fixtures installed on spindle.

This change in perspective allows the spatial coordinates of the platform joint centers to be determined. This change in perspective is achieved by expressing each ${}^M(\text{SM})_{j,i}$ in the PR system.

$${}^{PR}(SM)_{j,i} = ({}^{PR}T_M)_{j,i} {}^M(SM)_{j,i}$$

The coordinates ${}^{PR}(SM)_j$ are fit to the equation of a sphere by least squares (Appendix B). Assuming perfect spherical motion, the center of the best fit sphere is coincident with the center of rotation of the j^{th} strut platform joint. Hence the coordinates of the location of the j^{th} strut platform joint center (${}^{PR}P_j$) are the coordinates of the best-fit sphere center.

3.4 Locating the Spindle Nose

Once the location of the platform joint centers are known, the location and orientation of the spindle nose relative to the platform joint locations may be determined. This is done by tracking the rotation of the spindle relative to the P system.

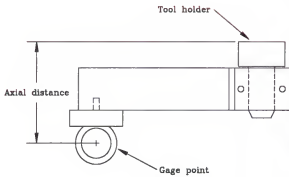
3.4.1 Spindle Fixture

A stiff fixture holding a gage point (SR) is attached to a tool holder. The axial offset distance of the tool holder gage point relative to the tool holder-spindle flange interface is determined externally by a CMM (Figure 3.11). The tool holder/fixture assembly is inserted into the spindle.

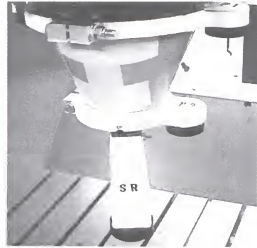
3.4.2 Data Collection

3.4.2.1 Before spindle rotation

The platform is held in a fixed pose from which the measuring device can reach the PR gage points and SR. The coordinates of the PR gage points are each measured several times, averaged and the coordinate transformation ${}^{Md}T_{PR}$ is calculated (Appendix A).



(a)



(b)

Figure 3.11 (a) Tool holder fixture; (b) Fixture installed on Hexel Tornado 2000.

3.4.2.2 During spindle rotation

The spindle is rotated slowly by hand. At approximately 30-40 locations uniformly distributed around several rotations (Figure 3.12), the spindle is stopped, and the coordinates the gage point F are measured relative to the M_d system (^{M_d}SR).

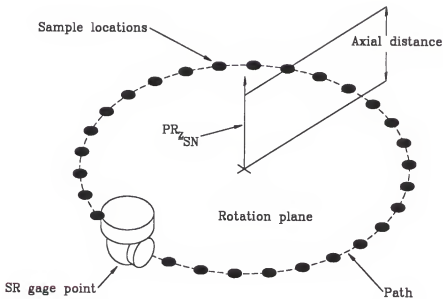


Figure 3.12 Spindle gage point path and sample strategy.

The coordinates ${}^{Md}SR$ are transformed into ${}^{PR}SR$:

$${}^{PR}SR = ({}^{Md}T_{PR})^{-1} {}^{Md}SR$$

3.4.3 Recovery of Spindle Parameters

Assuming that the spindle exhibits negligible axial and radial motion, the coordinates ${}^{PR}SR$ are fit to a skew circle (Appendix B). The unit normal vector of the best-fit plane is the unit orientation vector of the spindle relative to the P system (${}^{PR}z_{Sn}$). The coordinates of the center of the circle projected along the positive direction of the normal vector by the offset distance are the coordinates of the center of the spindle nose (revisit Figure 3.12).

3.4.4 Express Platform Joint Locations Relative to Spindle Nose

It is convenient to express the location of the platform joint locations relative to the spindle nose rather than vice versa. The appropriate coordinate transformation may be calculated by the following steps.

1. Compute the angle ϕ between the ${}^{PR}z_P$ and ${}^{PR}z_{Sn}$:

$$\phi = \arccos({}^{PR}z_P \cdot {}^{PR}z_{Sn})$$

2. Compute the normal vector \underline{n} from the cross product of ${}^{PR}z_P$ and ${}^{PR}z_{Sn}$:

$$\underline{n} = {}^{PR}z_{Sn} \times {}^{PR}z_P$$

3. Compute the rotation matrix ${}^{Sn}R_P$ from a rotation ϕ degrees about \underline{n} (Appendix A)
4. Compute the coordinate difference between ${}^{PR}P_o$ and ${}^{PR}S_{No}$:

$$\underline{\Delta Origin} = {}^{PR}P_o - {}^{PR}S_{No}$$

5. Assemble coordinate transformation:

$${}^{S_n}T_P = \begin{bmatrix} {}^{S_n}R_P & \underline{\Delta\text{Origin}} \\ 0 & 0 & 0 & 1 \end{bmatrix}$$

3.5 Determining Strut Lengths

Two different components of the strut length must be determined - the initialized strut lengths, and the variation of extension error of each strut. Accurate knowledge of the base and platform joint locations can now be leveraged to determine both the initial strut lengths, and the strut length error maps.

3.5.1 Initial Strut Lengths

Calculating the initial strut reference lengths proceeds as follows. The homing routine is executed. With the platform retracted at its home position, the coordinates of the PR gage points are measured relative to the M_d system. The coordinate transformations $({}^{M_d}T_{PR})_1$ and $({}^M T_{PR})_1$ are calculated. Knowing the locations of the base joints ${}^M B$ and location of the platform joints transformed into the M system ${}^M P$, the distances between the each of the six strut joint pairs $(L_{init})_{j=1 \text{ to } 6,1}$ are calculated from the formula for straight line distance. The platform is then moved from its home location, and the process is repeated. The i^{th} initial length for the j^{th} strut is denoted $(L_{init})_{j,i}$. This process is performed several times. The initial strut reference length for each strut is taken to be the mean of the calculated strut lengths for each strut over all of the trials.

3.5.2 Strut Length Error Tables

A procedure similar to the initial strut length identification is used to determine the forward and reverse strut length positioning errors.

3.5.2.1 Forward strut length measurements

The platform of the machine is sent to its home position. While the machine is at home, the coordinates of the PR gage points are measured, the coordinate transformations $({}^{Md}T_p)_1$ and $({}^M T_p)_1$ and the strut lengths are calculated $(L_{fwd})_{j=1 \text{ to } 6,0}$. All of the struts are lengthened equally by a nominal amount ΔL , and the measurement-calculation cycle is performed again. The i^{th} forward length for the j^{th} strut would be denoted $(L_{fwd})_{j,i}$. This sequence of extending the struts, and calculating the lengths continues until the maximum strut extension is reached (Figure 3.13).

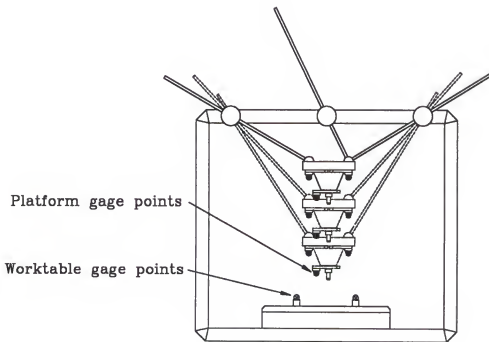


Figure 3.13 Forward and reverse strut length measurements.

3.5.2.2 Reverse strut length measurements

A reversal move is executed by extending all of the struts an additional amount ΔL and immediately retracting by ΔL . The platform pose measurement and strut length calculation is performed as in the forward strut length measurement procedure. The i^{th} measurement for the j^{th} strut is denoted $(L_{\text{rev}})_{j,i}$. Each strut is then retracted by ΔL and the measurement and strut length calculation cycle is performed. This process of retraction, measurement and strut length calculation continues until the platform reaches its home position.

3.5.2.3 Calculation of strut length positional errors

At this point, the lengths of all of the struts have been calculated for $2n$ poses - n poses forward and n poses reverse. Now the error in the strut extension must be calculated. First the initial strut lengths are subtracted from the sets of calculated strut lengths. Then the nominal displacement amounts are subtracted. The residual from these two calculations is the amount of positional error present in each of the struts at each displacement increment.

$$\begin{aligned} (e_{\text{fwd}})_{j,i} &= (L_{\text{fwd}})_{j,i} - (L_{\text{fwd}})_{j,1} - i \cdot \Delta L & j &= 1 \text{ to } 6 \\ (e_{\text{rev}})_{j,i} &= (L_{\text{rev}})_{j,i} - (L_{\text{fwd}})_{j,1} - (n - i + 1) \cdot \Delta L & i &= 1 \text{ to } n \end{aligned}$$

CHAPTER 4

UNCERTAINTY ANALYSIS

In order to determine how well the kinematic parameters can be determined for a particular machine and measuring instrument combination, it is necessary to perform an uncertainty analysis. The uncertainty analysis has two parts. The first part is to estimate how accurately the recovered parameters may be determined given the uncertainties present in the machine's strut assemblies and the spatial coordinate measuring instrument. The second is to analyze and understand the impact the estimated parameters will have on the machine's positioning performance. The candidate machine is a Hexel Tornado 2000 milling machine. Although the error budget presented here is prepared specifically for this machine, the same technique may be applied to all Stewart platform devices.

4.1 Strut Extension Error Budget

The cornerstone of the sequential determination method described in Chapter 3 is the accurate determination of the locations of all of the platform and base joints. The key to the process is to hold the strut length fixed between the base joint and the strut fixture, and between the platform joint and the strut fixture. In order to determine the uncertainty in the joint positions, it is necessary to determine the amount of uncertainty present in the length of each half of the strut above and below the strut gage point fixture.

4.1.1 Base Joint Strut Length Uncertainty

Factors which influence the length of the top half of the strut between the fixture and the center of rotation of the base joint are: base joint motion sphericity, strut axial flexibility, thermal effects, strut length command mismatch, and the least count servo motion.

4.1.1.1 Base joint motion sphericity

The base joints on the Hexel machine are a captured sphere design. A spherical shell containing the servo motor, encoder and drive nut, is constrained between two capturing rings. The separation between the capturing rings is adjusted to just allow the trapped sphere to rotate freely between the rings without binding. The factors which govern the sphericity of the motion of the joint are the nonspherical form of the ball, and imperfections in the surfaces of the ball and the capturing ring seats. These imperfections may cause the center of the sphere to move during the joint's motion. This unwanted nonspherical motion when projected into the strut line of action during motion, causes the strut to lengthen or shorten. This effect can be thought of as a shim of thickness "t" wedged between the sphere and the seat (Figure 4.1).

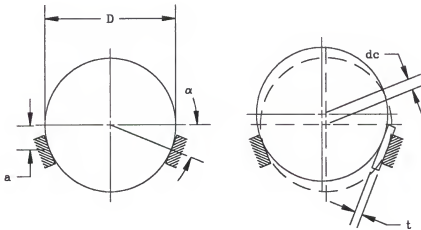


Figure 4.1 Effect of joint nonsphericity on joint center location.

From the diameter of the sphere “D”, the seat location “a”, and the shim thickness “t” the amount of motion the joint center experiences “dc” may be calculated.

$$\alpha = \operatorname{atan}\left(\frac{2a}{D}\right) \quad dc = \frac{t}{\sin(2\alpha)}$$

CMM measurement of the joint spheres and ring seats show the sphericity of the Hexel base joints to be 0.020mm. Knowing D=153mm, and a=38mm a total motion of the joint center of approximately 0.025mm is expected which is approximately the sphericity of the joint motion. However, it is important to note that this is the total motion between the lowest point on the sphere to the highest. The nominal sphere surface is approximately in the middle of this range. Therefore the expected motion range of the screw would be ± 0.013 .

4.1.1.2 Mechanism flexibilities

The stiffness of parallel platform machines and the axial strut loads are directly dependent upon the geometry of the particular pose in which the machine is placed (Appendix C). During any move, the geometry of the machine is continually changing, which means the machine stiffness and strut loadings are changing. The combination of varying loads and changing stiffness may cause the structure to deform even under static conditions (Figure 4.2). Knowing the geometric and material properties of the struts, the mass of the platform, and the paths the mechanism is to traverse, the average deflection of the 800mm fixed length strut is calculated (Appendix C) to be approximately ± 0.005 mm. Since the strut fixture is connected at the midpoint of the strut, the uncertainty is approximately ± 0.003 mm for the base joint half the strut.

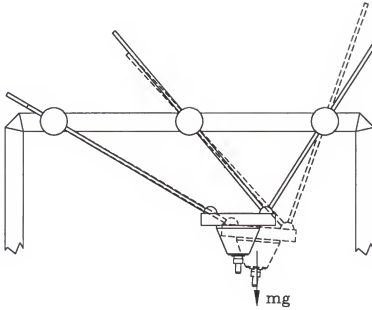


Figure 4.2 Effect of mechanism flexibility.

4.1.1.3 Thermal sources

The Hexel struts are straight, long, thin and hollow (30mm O.D., 19mm I.D. 800mm in total fixed length) making them susceptible to changes in the ambient air temperature. The approximate measurement cycle time for each strut is 45-60 minutes. Due to the long and thin construction of the struts, it is likely the changes in the ambient air temperature will affect the total length of the strut during the measurement cycle (Figure 4.3).

The amount of length change in the strut can be estimated from the length of the strut (L), the coefficient of thermal expansion for the strut material (α), and the largest temperature deviation expected to occur during the measurement cycle (ΔT_{amb})

$$\Delta L_{th} = L\alpha\Delta T_{amb}$$

The struts are made from 304 stainless steel ($\alpha=0.0000173$ mm/mm/°C). The distance between the base joint and strut fixture is approximately 400mm. The room in which the machine is housed is temperature controlled to $\pm 1^\circ\text{C}$. The calculated deviation in the strut length due to an ambient temperature change during the measurement cycle is approximately ± 0.007 mm.

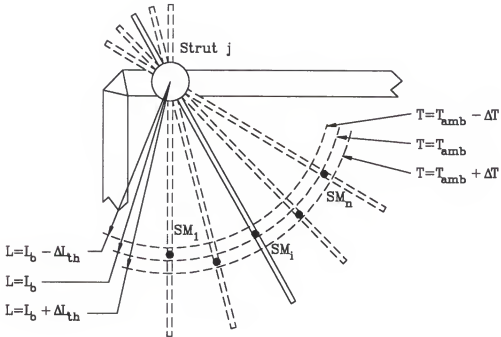


Figure 4.3 Effect of temperature change on strut length.

4.1.1.4 Strut length command mismatch

The Hexel is not capable of interpreting a motion control program constructed solely of strut lengths, however it does interpret M/G codes. Therefore in order to hold a strut at a desired fixed length, it is necessary to design a motion control program to guide the spindle nose such that the strut in question stays at the desired length (Appendix C). This requires that the model used inside the controller and the path planner match exactly. It

does not matter whether the kinematic parameters for the model accurately reflect the construction of the particular machine, only that the same kinematic parameters are used in both the machine and the path planner. However, small differences between the desired and actual commanded length of the strut arise from slight differences in the way the controller and simulation models operate. These small differences can be detected experimentally by observing the deviation between the desired and the actual commanded strut length displayed on the controller's readout. During trial runs of the motion programs on the Hexel, the difference between the desired and the actual commanded strut length amounted to approximately $\pm 0.005\text{mm}$.

4.1.1.5 Encoder resolution

Most servo driven mechanisms use an encoder to measure the position, velocity and the direction of motion of the joint axes. A pulse is generated only after the axis has moved by the scale's least count, which means it is possible for the axis to move between two encoder pulses without the controller ever registering motion (Figure 4.4). For screw driven axes with rotary encoders this is calculated from the pitch of the screw (p) and the angular resolution of the encoder disk ($\Delta\theta$):

$$\Delta L_{lc} = p_{screw} \Delta\theta$$

The servo motors on the Hexel milling machine use 10,000 count interpolated encoders and have a thread pitch of 5mm, resulting in a linear resolution of $\pm 0.0005\text{mm}$.

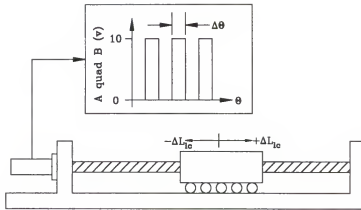


Figure 4.4 Effect of encoder least count on joint center location.

4.1.1.6 Strut bending

In Chapter 3, the strut fixture and measurement strategy was tailored specifically to eliminate measurement errors from the collected strut gage point coordinate data due to joint friction induced strut bending. This was achieved by calculating the coordinates of a point (SM) on or very near to the neutral axis of the strut from the measured coordinates SA and SB equidistant from each other across the centerline of the strut. Although the strut may still bend during motion, the amount of radial motion the point on the neutral axis relative to the joint center is negligible, and will not be included in the calculation of the strut length uncertainty.

4.1.1.7 Computation of base joint strut length uncertainty

Tabulating the uncertainties in the length of the top half of the fixed length strut (approximately 400mm), the total uncertainty is computed by taking the root-sum-squares (RSS) of all of the contributing uncertainties (Table 4.1).

Table 4.1 Length uncertainty in base joint strut section.

Uncertainty Component	Value (mm)
Base Joint Sphericity	± 0.013
Strut Flexibility	± 0.003
Thermal Effects	± 0.007
Command Mismatch	± 0.005
Least Count Motion	± 0.001
RSS	± 0.016

4.1.2 Platform Joint Strut Length Uncertainty

Factors which influence the length of the bottom half of the strut between the strut fixture and the center of rotation of the corresponding platform joint are: platform joint motion sphericity, strut axial flexibility and thermal effects.

4.1.2.1 Platform joint motion sphericity

The platform joints for the Hexel are a bifurcated magnetic ball and socket joint design, where two struts are connected to a single ball and socket joint. One strut is connected to a solid sphere, which is held in a spherical cup attached to the platform by a powerful magnet. The second strut is connected to the solid sphere by a pivot bearing located at the center of the sphere, with the axis of rotation normal to the centerline of the other strut. Since the motion of this type of joint is complicated to analyze, it will be treated as if each strut is connected to its own magnetic ball and socket joint at a coincident point. The spherical motion of the joint is governed by the sphericity of the spheres in the magnetic cups. As in the case of the base joints, the small nonspherical motion of the joint is projected into the strut's line of action, which causes the strut to appear to increase

and decrease in length. However, if the rotation axis of the dependent strut connected to the solid sphere does not pass through the center of the sphere, the resulting motion of the dependent strut will have a larger sphericity error. The sphericity measured by a CMM at SNL was reported to be 0.025mm.

4.1.2.2 Mechanism flexibilities

Since the length between the platform joints and the strut fixture is approximately the same as the base joint to the strut fixture, the average axial deflection due to imparted axial strut loading is also approximately the same, which is $\pm 0.003\text{mm}$.

4.1.2.3 Thermal sources

Since the length between the platform joints and the strut fixture is approximately the same as the base joint to the strut fixture, the average axial deflection due to thermal effects is also approximately the same, which is $\pm 0.007\text{mm}$.

4.1.2.4 Computation of platform joint strut uncertainty

Tabulating the uncertainties in the length of the bottom half of the fixed length strut (approximately 400mm in length), the total uncertainty is computed by taking the root-sum-squares of all of the contributing uncertainties (Table 4.2).

Table 4.2 Length uncertainty in platform joint strut section.

Uncertainty Component	Value (mm)
Platform Joint Sphericity	± 0.013
Strut Flexibility	± 0.003
Thermal Effects	± 0.007
RSS	± 0.015

4.2 SMX 4000 Laser Tracker Error Budget

The objective of this work is not to create an error budget for a laser tracker. Therefore information regarding its measurement uncertainty must be determined in some other way. The uncertainty in the target position reported by the SMX 4000 laser tracker is approximately 0.025mm (according to SMX engineers). The reported position is within a 0.050mm diameter sphere centered about the actual position.

4.3 Propagated Uncertainty in Recovered Parameters

4.3.1 Uncertainty Scenarios

Four different uncertainty scenarios will be explored. Scenario #1 is intended to be a realistic case reflecting the uncertainties in the strut length and measurements estimated to occur in the actual experiment (Chapter 5). Scenario #2 is intended to show how the realistic machine uncertainty alone affects the identification process. Scenario #3 is intended to show how measurement error alone contributes to the uncertainty in the identification process. Scenario #4 is intended to be an optimistic case of scenario #1 with smaller positioning and measurement uncertainties. Table 4.3 shows the differing input uncertainties associated with each scenario.

Table 4.3 Scenario input uncertainties.

Scenario	Base Section (mm)	Platform Section (mm)	Measurement (mm)
1	0.016	0.015	0.025
2	0.016	0.015	0.000
3	0.000	0.000	0.025
4	0.010	0.010	0.013

4.3.2 Monte Carlo Simulation Process

Figure 4.5 shows the flowchart for the entire simulation process. Each scenario will be subjected to 10000 iterations. For each iteration, different amounts of measurement and machine uncertainty will be introduced, and a new set of joint center locations and initial strut lengths will be calculated.

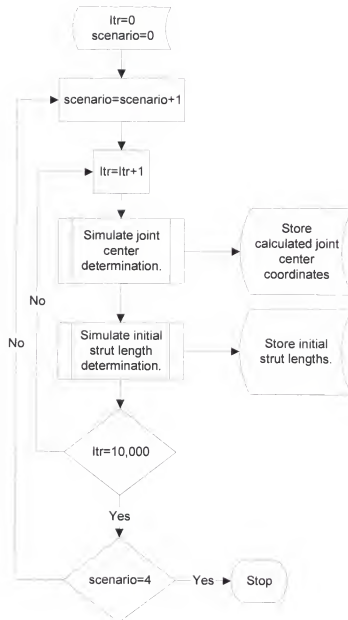


Figure 4.5 Flowchart for the Monte Carlo simulation process.

4.3.3 Joint Center Computation

Figure 4.6 shows the flowchart for the joint center determination subtask of the simulation process. The set of nominal kinematic parameters and an appropriate tool path for the particular strut are given to the reverse kinematic solver which calculates the strut lengths for each pose in the toolpath. A small amount of random strut length uncertainty is added to the strut lengths. The new pose of the platform and gage point locations are calculated. Random measurement uncertainty is added to the gage point locations. Finally, the joint center locations are determined from these perturbed gage point locations.

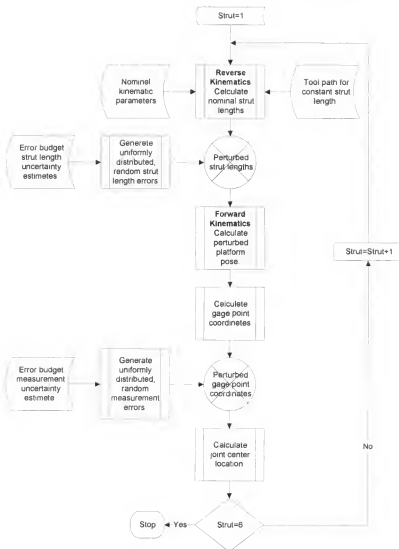


Figure 4.6 Flowchart for simulation loop.

4.3.4 Initial Strut Length Computation

Figure 4.7 shows the flowchart for the initial strut length computation subtask of the simulation process. It is nearly the same as the joint center computation subtask with the exception that it is executed only once for all six struts and the toolpath holds the platform at the home position.

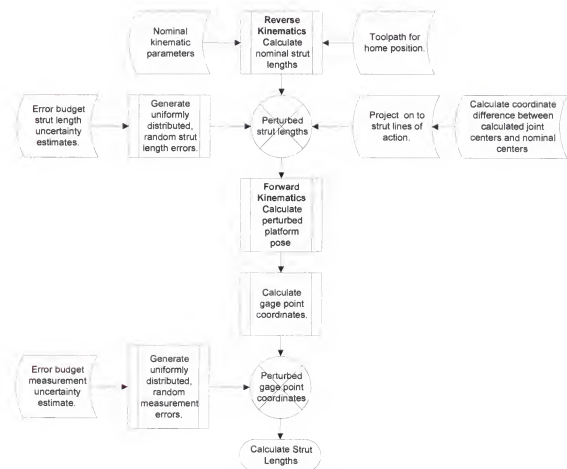


Figure 4.7 Flowchart for simulation loop.

4.3.5 Calculated Joint Location Quality

Using the uncertainty in the strut lengths and the Monte Carlo method, the potential accuracy of the joint locations can be determined. There are two values which are of inter-

est when considering the accuracy of a spherical fit: sphericity and the center error distance.

4.3.5.1 Sphericity of fit

Sphericity is defined as the maximum distance between the collected data points “ D_j ” and the best-fit sphere center $(h,k,l)_j$ minus the minimum distance between the collected data points and the best-fit sphere center for the j^{th} strut (Figure 4.8).

$$\text{Sph}_j = \max \left(\sqrt{(D_{x,j} - h_j)^2 + (D_{y,j} - k_j)^2 + (D_{z,j} - l_j)^2} \right) - \min \left(\sqrt{(D_{x,j} - h_j)^2 + (D_{y,j} - k_j)^2 + (D_{z,j} - l_j)^2} \right)$$

$j = 1 \text{ to } 6$

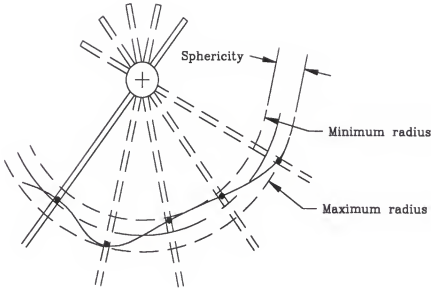


Figure 4.8 A two-dimensional depiction of sphericity

Logic would dictate that the smaller the sphericity, the better the spherical fit and the closer the recovered coordinates of the sphere center are to the real value. Data creating a perfect sphere would have a $\text{Sph}=0$. However, sphericity gives no indication of how close the best-fit center coordinates are to the actual coordinates. It would seem possible to have

a high sphericity value and still recover an accurate value for the sphere center, and vice-versa. Even though sphericity does not directly yield information on the accuracy of the center recovery, it is a property of the data fit which can be easily calculated and compared. It may be possible to formulate through the Monte Carlo process a relationship between sphericity and the error distance between the calculated sphere center and the nominal sphere center.

4.3.5.2 Center error distance

The center error distance (CED) is the distance between the nominal value of the joint center and the best-fit sphere center (Figure 4.9).

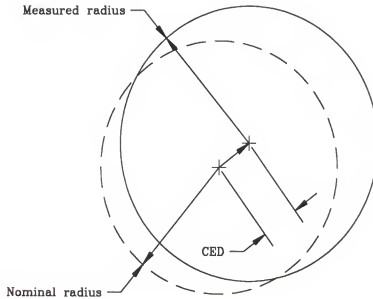


Figure 4.9 Depiction of the center error distance.

This quantity is not directly measurable since in most cases the actual location of the joint center is not known. It therefore becomes impossible to directly compare the experimentally determined joint center coordinates to the known values. Through the Monte Carlo method, it may be possible to determine a range of sphericity values which would

statistically tend to yield acceptable values for the CED and infer an accurate determination of the joint center location. This same relation may also be used to determine a range of possible CED's for a specific, experimentally determined sphericity value.

$$CED_j = \sqrt{(h_{nom,j} - h_j)^2 + (k_{nom,j} - k_j)^2 + (l_{nom,j} - l_j)^2} \quad j = 1 \text{ to } 6$$

4.3.6 Joint Center Location Uncertainty

4.3.6.1 Joint location toolpaths

Each of the struts requires a unique path plan to keep the particular strut at a constant length during measurement. The feasible motion regions were determined in a computer simulation for a level platform by testing discrete points over a 50mm x 50mm grid on the surface of each 800mm sphere for strut extension length violations and measuring instrument reachability. Originally, these regions were calculated for use with the Laser Ball Bar (LBB) before it was decided to use the two-gage point strut fixture and the laser tracker. New feasible motion regions were not recalculated for specific use with the tracker. All of the paths contain 20 points, picked using engineering judgement from the feasible motion regions (Figures 4.10).

4.3.6.2 Simulation CED results

In Table 4.3 the effects of the four uncertainty scenarios on the mean CED over 10000 iterations for each of the six struts are shown. This table shows the mean CED distances from the nominal joint center for the respective input uncertainty scenario calculated for both the base and the platform joints.

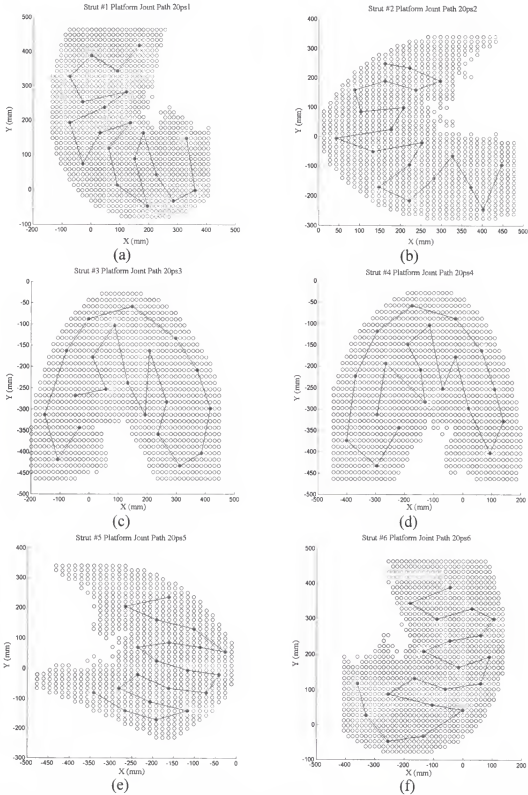


Figure 4.10 Constant strut length toolpaths: (a) Strut 1, (b) Strut 2, (c) Strut 3, (d) Strut 4, (e) Strut 5, (f) Strut 6.

Table 4.3 Results of the Monte Carlo joint identification simulations for CED (mm).

Strut Number	Scenario Number	Base Joint		Platform Joint	
		Mean (mm)	σ (mm)	Mean (mm)	σ (mm)
1	1	0.067	0.044	0.098	0.064
	2	0.048	0.031	0.045	0.028
	3	0.050	0.032	0.086	0.057
	4	0.039	0.025	0.054	0.035
2	1	0.071	0.047	0.118	0.078
	2	0.050	0.032	0.047	0.030
	3	0.052	0.034	0.110	0.072
	4	0.041	0.027	0.065	0.043
3	1	0.063	0.041	0.083	0.054
	2	0.044	0.028	0.041	0.027
	3	0.045	0.030	0.071	0.046
	4	0.036	0.024	0.046	0.030
4	1	0.069	0.046	0.090	0.059
	2	0.048	0.032	0.046	0.030
	3	0.051	0.034	0.077	0.051
	4	0.040	0.026	0.050	0.033
5	1	0.115	0.079	0.193	0.136
	2	0.080	0.054	0.075	0.051
	3	0.082	0.056	0.178	0.125
	4	0.066	0.045	0.105	0.074
6	1	0.079	0.053	0.108	0.072
	2	0.054	0.036	0.051	0.033
	3	0.056	0.038	0.096	0.064
	4	0.045	0.029	0.060	0.040

In all of the scenarios except #2, the platform joint center has a higher mean CED than the base joint. Considering the pose of the platform is measured relative to the machine system, this is not a surprising result. The associated uncertainty in the platform pose measurement directly couples into the transformed data which is used in the data fitting routine to determine the platform joint center location. The results for strut 5 are

approximately twice as large as those of the other struts. This appears to be a problem with the path chosen for strut 5. The objective of this research was not to minimize the error in the recovered parameters. The topic of path planing will be discussed in the Future Work section in chapter 6.

4.3.6.3 Sphericity results

Table 4.4 shows the results for sphericity for the respective input uncertainty scenario for the base and the platform joints for each strut. In all of the scenarios except scenario #2, the platform joint center has a higher mean sphericity than the base joint for the same reason as explained for the mean CED distance. Note that when the measurement uncertainty is zero in scenario #2, the sphericity is slightly less than that of the base joint again since the platform half of the strut has less uncertainty than the base half.

It would seem suspicious that the results for the sphericity of the base joints are so consistent between the differing strut toolpaths. After carefully checking the computer code and finding no errors in its execution, the only other explanation lies in the construction of the toolpaths themselves. Looking back at the graphs of toolpaths in Figure 4.10, it can be seen that all of the paths are contained in similar cone angles relative to the joints in question. This leads to the possibility that since the paths had the same number of points and roughly the same distribution over similar cone angles, similar results may be expected for both the sphericity and the CED, which is evident from the results in Table 4.3 and 4.4. The platform CEDs and sphericities are not as consistent as the base joint CEDs and sphericities, possibly due to the introduction of the measurement error in the platform pose. This is evident from the fact that the CEDs and sphericities are very consistent between scenario #2 results.

Table 4.4 Joint identification simulation results for sphericity (mm).

Strut Number	Scenario Number	Base Joint		Platform Joint	
		Mean (mm)	σ (mm)	Mean (mm)	σ (mm)
1	1	0.045	0.008	0.064	0.014
	2	0.029	0.004	0.027	0.003
	3	0.033	0.006	0.057	0.013
	4	0.026	0.005	0.035	0.007
2	1	0.045	0.008	0.077	0.017
	2	0.029	0.004	0.027	0.003
	3	0.033	0.006	0.072	0.016
	4	0.026	0.005	0.042	0.009
3	1	0.045	0.008	0.059	0.012
	2	0.029	0.004	0.027	0.003
	3	0.033	0.006	0.051	0.011
	4	0.026	0.005	0.033	0.006
4	1	0.045	0.008	0.059	0.012
	2	0.029	0.004	0.027	0.003
	3	0.033	0.006	0.051	0.011
	4	0.026	0.005	0.033	0.007
5	1	0.045	0.008	0.075	0.016
	2	0.029	0.004	0.027	0.003
	3	0.032	0.006	0.069	0.016
	4	0.026	0.005	0.041	0.009
6	1	0.045	0.008	0.063	0.014
	2	0.029	0.004	0.027	0.003
	3	0.033	0.006	0.056	0.012
	4	0.026	0.005	0.035	0.007

4.3.6.4 Graphical representations of CED and sphericity distributions

The results for the joint identification procedure for each run have been compiled in Tables 4.3 and 4.4, but it is desirable to see the distributions of the results graphically. Figures 4.11-4.14 show the results for the CED and the sphericity for strut 1. For each run, two sets of three graphs (three for the base joint, three for the platform joint) were pro-

duced to display the distribution of the calculated CEDs and sphericities over all of the iterations.

Plots (a) and (d) are overhead views of surface plots of the distribution of the CED versus sphericity. This view is useful to determine an expected range for the CED given a sphericity. For example, if an experiment were conducted for a base joint under the conditions of scenario #1, the expected sphericity should lie in the range 0.035-0.060mm. Knowing the range of expected sphericity enables the user to estimate the identified joint center would be between 0-0.15mm away from the actual joint center location. If the experiment were conducted, yielding a sphericity result of 0.035mm, the chart would allow the user to estimate that the distance from the actual joint center is between 0.03-0.08mm away from the identified joint center.

Plots (b) and (e) are the distributions of the CED calculated over all of the 10000 iterations. The dotted line in these graphs depicts the mean. From this plot the success of the identification procedure becomes more obvious. A perfect estimation of the location of the joint center occurs when the CED is equal to zero. This allows the effects of the measurement and machine position uncertainties to be seen and compared. Using this graph before conducting the experimental procedure allows the measurement process to be fine tuned.

Plot (c) and (f) are the distributions of the calculated sphericities over all of the 10000 iterations. The dotted line in these graphs depicts the mean. This plot may be used as a diagnostic graph leading up to the joint identification measurement process, allowing the user to determine in advance the range of expected sphericities given the total amount of uncertainty estimated to be present in the measurements.

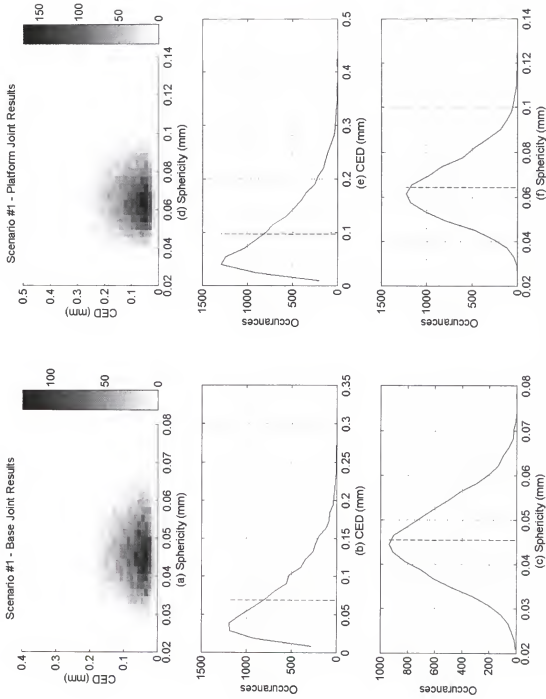


Figure 4.11 Strut 1, scenario #1 - CED and Sphericity results: (a-c) Base joint, (d-f) Platform joint.

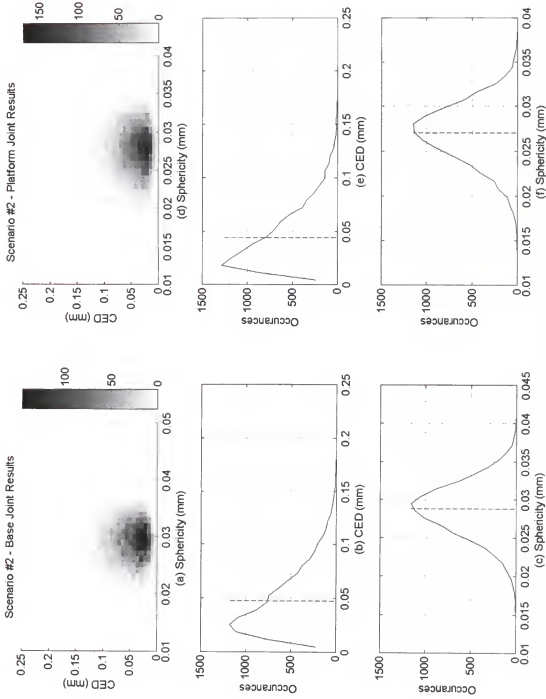


Figure 4.12 Strut 1, scenario #2 - CED and Sphericity results: (a-c) Base joint, (d-f) Platform joint.

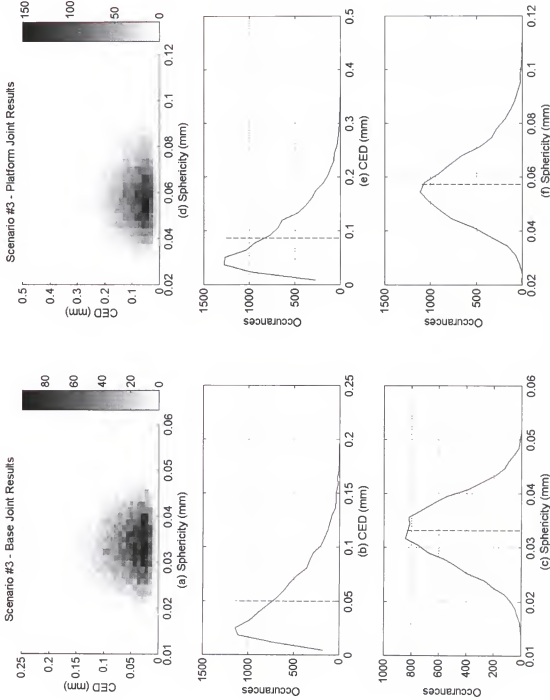


Figure 4.13 Strut 1, scenario #3 - CED and Sphericity results: (a-c) Base joint, (d-f) Platform joint.

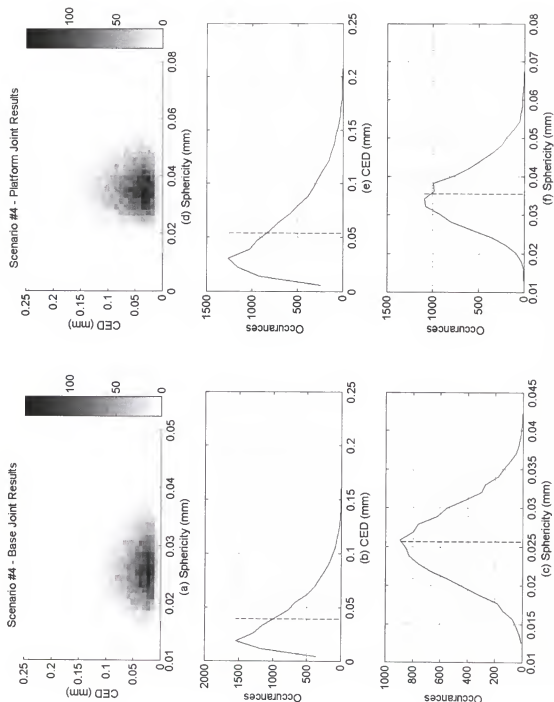


Figure 4.14 Strut 1, scenario #4 - CED and Sphericity results: (a-c) Base joint, (d-f) Platform joint.

4.3.7 Strut Length Uncertainty

The uncertainty in the initial strut length was also calculated over the 10000 iteration Monte Carlo simulation for each scenario and strut combination. These results appear in Table 4.5. Since the value of the initial strut lengths are dependent upon the locations of the limit switches on each individual strut, the mean value of the strut length in simulation is essentially meaningless. However, the standard deviations of the initial strut lengths gives a good account of how well the target initial strut length may be repeated during the simulations.

Table 4.5 Initial strut length uncertainty results

Scenario	$\sigma_{\text{Strut 1}}$ (mm)	$\sigma_{\text{Strut 2}}$ (mm)	$\sigma_{\text{Strut 3}}$ (mm)	$\sigma_{\text{Strut 4}}$ (mm)	$\sigma_{\text{Strut 5}}$ (mm)	$\sigma_{\text{Strut 6}}$ (mm)
1	0.139	0.162	0.122	0.134	0.287	0.160
2	0.066	0.071	0.060	0.067	0.123	0.076
3	0.123	0.147	0.106	0.118	0.257	0.141
4	0.077	0.089	0.067	0.075	0.157	0.088

Measurement uncertainty again is a large contributor as the results of scenarios #2 and #3 show. The results for scenario #2 are by far lower than any other which leads one to believe that measurement uncertainty is much more detrimental to the performance of the sequential determination method than machine uncertainty.

4.4 Propagated Uncertainty in Machine Positioning

4.4.1 Calculating Uncertainty in a Path

Knowing all of the uncertainties in the joint locations and strut lengths, a Monte Carlo simulation may be designed to test how these uncertainties affect the position of the tool

tip. First, a path plan is developed for the tool tip to follow. Second, using the nominal joint locations, the inverse kinematics are used to determine the pose of the mechanism at selected places on the path. Third, joint location and initial strut lengths from an identification simulation are used. At each point on the path the initial length errors and joint center errors are projected onto the strut lines of action to find the strut length errors. Other machine error are then added (the strut length uncertainties calculated at the beginning of this chapter) to further perturb the strut length at each joint. The error projected on the strut length are used in the forward solution to determine the perturbed pose of the platform. This disturbance process is performed for each point in the entire path. The path may then be analyzed to determine the performance of the mechanism after calibration.

4.4.2 Circular Trace

A series of circular paths will be used to test the machine after calibration. Using the aforementioned method for determining tool tip positional uncertainty, six circular traces of radius 150mm and 300mm, containing 360 points, are simulated for each of the four uncertainty scenarios (Table 4.7) for 1000 different simulated machine calibrations. These 1000 calibrations come from the 10000 calibration results stored from the kinematic parameter simulation discussed in the previous section.

The coordinates at the tool tip determined from the forward kinematics for each of the 360 points in the path are fit to a skew circle. Over all of the 1000 traces for each circle location under each uncertainty scenario, the mean and standard deviation about the mean of the X and Y circle center coordinates, radii and circularities are calculated (Table 4.8).

Table 4.7 Circular trace workspace positions.

Circle Number	Nominal Center Position (mm)			Nominal Radius (mm)
	X	Y	Z	
1	0	0	180	150
2	200	200	180	150
3	-200	200	180	150
4	-200	-200	180	150
5	200	-200	180	150
6	0	0	180	300

Table 4.8 Results of circular path simulations for all uncertainty scenarios.

Scenario	Circle	\bar{X}	σ_X	\bar{Y}	σ_Y	\bar{R}	σ_R	$\bar{Circ.}$	σ_{Circ}
		(mm)	(mm)	(mm)	(mm)	(mm)	(mm)	(mm)	(mm)
1	1	0.000	0.038	0.001	0.038	150.000	0.002	0.115	0.008
2	1	-0.001	0.018	0.000	0.018	150.000	0.001	0.115	0.008
3	1	0.001	0.033	-0.001	0.032	150.000	0.001	0.003	0.002
4	1	-0.001	0.021	0.000	0.021	150.000	0.001	0.074	0.005
1	2	200.000	0.035	200.003	0.035	150.000	0.002	0.130	0.009
2	2	200.000	0.017	200.000	0.017	150.000	0.001	0.131	0.009
3	2	200.000	0.032	200.000	0.030	150.000	0.001	0.003	0.002
4	2	199.999	0.020	200.000	0.019	150.000	0.001	0.084	0.006
1	3	-200.001	0.038	200.000	0.039	150.000	0.002	0.131	0.010
2	3	-200.000	0.019	200.001	0.019	150.000	0.002	0.130	0.009
3	3	-199.999	0.034	200.000	0.033	150.000	0.001	0.003	0.002
4	3	-200.001	0.021	200.000	0.022	150.000	0.001	0.084	0.006
1	4	-200.000	0.035	-200.001	0.038	150.000	0.002	0.125	0.009
2	4	-200.000	0.016	-200.000	0.019	150.000	0.001	0.125	0.009
3	4	-199.998	0.030	-200.002	0.032	150.000	0.001	0.003	0.002
4	4	-200.000	0.019	-199.999	0.021	150.000	0.001	0.081	0.006
1	5	200.000	0.037	-199.999	0.032	150.000	0.002	0.125	0.009
2	5	200.000	0.017	-200.000	0.015	150.000	0.001	0.125	0.009
3	5	200.001	0.032	-200.000	0.027	150.000	0.001	0.002	0.001
4	5	199.999	0.020	-200.000	0.017	150.000	0.001	0.081	0.006
1	6	0.000	0.036	0.001	0.034	300.000	0.003	0.122	0.008
2	6	-0.001	0.017	0.001	0.016	300.000	0.002	0.121	0.008
3	6	0.000	0.032	-0.001	0.029	300.000	0.002	0.005	0.003
4	6	-0.001	0.019	0.000	0.019	300.000	0.002	0.078	0.005

Scenario #3 appears to be the best overall. Scenario #3 assumes the machine is perfect, and the measuring instrument is in error. This yielded substantial uncertainty in the initial strut length (Table 4.5), yet the calibrated machine in simulation appears to trace all six circles accurately, but in the wrong places. This would seem to indicate that reasonably small constant initial strut length errors only shifts the desired path in space, but does not contribute to path distortion. It is important to keep in mind these circular paths were simulated relatively close to the worktable where the struts are extended to approximately 1m. Also, the platform was not rotated during the circular path traces. True multiaxis contouring moves over a wider range of motions may show different results and should be investigated further for future work.

Comparing scenarios #2 and #3 also shows that the uncertainty in the strut length is very detrimental to the performance of the machine. From these results it appears that one may conclude that accurate knowledge of the joint center to joint center strut length is of extreme importance since errors in strut length directly affect the location of the tooltip. Joint position errors on the other hand do not couple directly into the location of the tooltip since only a component of the error is projected into the strut line of action which affects the location of the tool tip which varies as the platform moves.

CHAPTER 5 VERIFICATION OF METHOD

A total of three complete and independent trials were run of the proposed sequential determination method on the Hexel machine installed at Sandia National Laboratories. This process yielded three new kinematic parameter sets. Each set was loaded into the Hexel's control computer, and was thoroughly tested. This section describes all of the equipment used, the results for the identified kinematic parameters, and the results of the diagnostic positioning performance measurements for each of the three trials.

5.1 Description of Equipment Used

5.1.1 Hexel Tornado 2000

This six-axis (five programmable) milling machine built in 1997 by Hexel Corporation in Hew Hampshire, is a 6-3 Stewart platform design, and is the test bed for the sequential determination technique presented in Chapter 3. It is installed at Sandia National Laboratories (SNL) in the Advanced Manufacturing Processes Laboratory in Albuquerque, NM (Figure 5.1). The Hexel Tornado 2000 has 1m travel in both the X and Y axes, and 0.5m travel in the Z axis. The amount of platform tilt varies throughout the workspace, but within a 0.5m x 0.5m area at the center of the workspace. It has a 17,000 RPM, 20kW spindle with an HSK 50 tool holder and can achieve 500ipm feedrates.

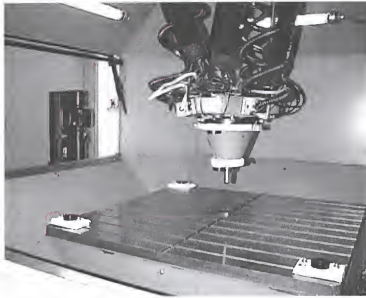


Figure 5.1 Hexel Tornado 2000 installed at SNL.

5.1.2 SMX 4000 Laser Tracker

A SMX 4000 Laser Tracker was used to collect the spatial coordinate data (Figure 5.2a). The SMX 4000 utilizes a heterodyne interferometer guided by two rotary axes to track a retroreflector target in space (Figure 5.2b). A laser beam is generated and split into two parts. One part is the reference beam, the other guided by two servo-controlled rotary axes is shot at the target. The target reflects the beam back on itself to the laser head. The reflected beam is interfered with the reference beam. The phase shift between the reference and the reflected beam is measured to detect motion in the direction of the laser beam. An array of electronics and photodiodes inside the tracker track the motion of the incident beam and create a error signal. This error signal drives the position of the servo motors. The positions of the encoders on the rotary axes are read to determine the direction of the laser beam. Using the distance and direction, the location of the target in space

may be calculated. According to SMX, the 4000 has a static measuring accuracy of 0.025mm.

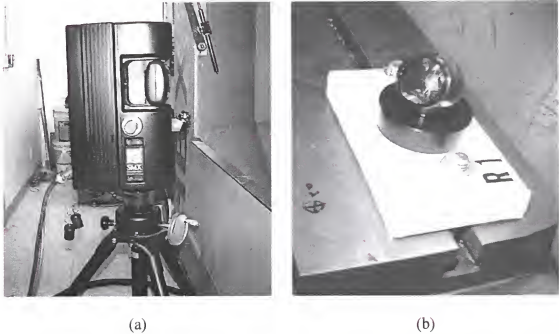


Figure 5.2 (a) SMX 4000 Laser Tracker on tripod, (b) retroreflector in kinematic nest.

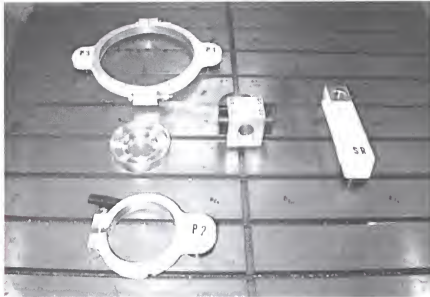
5.1.3 Fixtures Used

Several fixtures which hold the SMX target nests (gage points) were designed and fabricated (Figure 5.3a). These consist of three reference gage point fixtures, one two-piece spindle housing clamp for gage points PR_1 and PR_3 , one two-piece spindle nose clamp for gage point PR_2 , one two-piece strut clamp fixture for gage points SA and SB , and a tool-holder fixture for gage point SR . Figure 5.3b shows all of the platform fixtures installed on the spindle. Design drawings are shown in Appendix D.

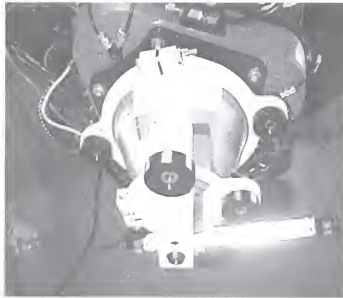
5.1.3.1 Central reference gage point fixtures

The three central reference gage point fixtures are bolted to the worktable top and provide a stable, stationary frame to which all data collected in various other reference frames

may be converted. Each fixture consists of a SMX target nest bolted to an insulated 6"x4"x1" 6061-T6 aluminum block. The fixture itself is bolted into the T-slots of the table by 2 - 5/8" steel bolts. The three reference fixtures appear in Figure 5.1. A close-up appears in Figure 5.4.



(a)



(b)

Figure 5.3 (a) Gage point fixtures, (b) Fixtures installed on spindle.



Figure 5.4 Close-up of reference gage point fixture.

5.1.3.2 Platform gage point fixtures

Two 6061-T6 aluminum fixture assemblies are used to attach the PR gage points to the platform. The first assembly holds gage points PR_1 and PR_3 . This assembly consists of two-part clamp which is affixed around the spindle housing near the platform. Two 1/2" bolts are used to tighten the two piece clamp around the spindle housing. Two SMX target nests are bolted to the underside of the fixture (Figure 5.3b). The fixtures holding the PR_2 gage point connect to the spindle nose. One piece mates with grooves existing in the spindle housing of the spindle nose and is secured to the spindle housing by six 3mm screws. The second part slips over the first and is clamped to the first by tightening a hand knob. All of the fixtures are insulated to protect against thermal distortion.

5.1.3.3 Strut gage point fixture

The two-piece strut fixture clamp is made of 6061-T6 aluminum (Figure 5.5). Two target nests are bolted to one half. The other half bolts to the first, clamping around the strut.

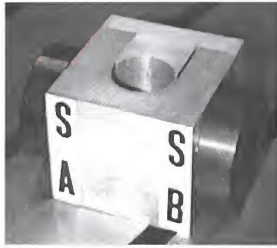


Figure 5.5 Close-up of reference strut gage point fixture.

5.1.3.4 Toolholder fixture

The toolholder fixture used to measure the axis of rotation of the spindle is simply an insulated 6061-T6 aluminum bar (Figure 5.3a and 5.3b). One end has a hole bored which slips over the toolholder. An SMX target nest is bolted to the other end (gage point SR).

5.1.4 Renishaw Ball Bar

The Renishaw Ball Bar is a diagnostic device used to test the health of a computer numerically controlled (CNC) machine tool. It consists of a precision LVDT length transducer mounted between two precision-ground spheres. One of the spheres is mounted to the worktable (Figure 5.6), while the other is seated in a magnetic kinematic mount held in the spindle of the machine tool. A circular path is commanded of the CNC machine. The ball bar then reads the variations in the radius of the circle as the machine tool executes the circular path. The data from the path is analyzed to determine the error motion of the machine from the nominal circle. The results of static or dynamic tests in orthogonal serial

axis machines can reveal problems such as ballscrew backlash, servo gain mismatches, and squareness errors between axes. The Renishaw ball bar is used in this work to make the first determination of the degree of success in properly identifying the correct kinematic parameters. A sample of the analysis output from the Renishaw appears in Figure 5.7 which was conducted using the trial 2 parameter set.

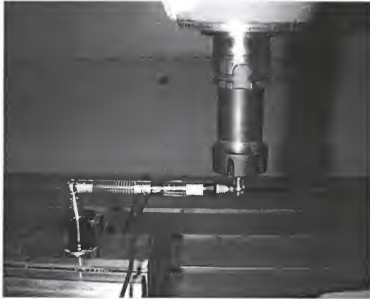


Figure 5.6 The Renishaw Ball Bar installed on the Hexel milling machine.

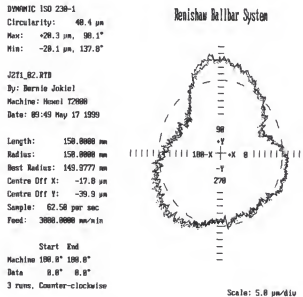


Figure 5.7 Sample output from Renishaw Ball Bar software.

5.2 Results: Joint Center Locations

5.2.1 Path Plans

Each of the struts requires a unique path plan to keep the particular strut at a constant length during measurement. The paths presented in section 4.3.6.1 (Figure 4.10) will be used during the experiments.

5.2.2 Rejection of Bad Data Points

A method of rejecting bad data points was needed to identify and remove measurements from the data sets which appeared to be inaccurately measured. This was accomplished by checking the invariant inter-target distance between the strut gage points, and the invariant inter-target distances between the platform gage points. For each pose, the distances SA-SB, pr_1 - pr_2 , pr_1 - pr_3 , and pr_2 - pr_3 were calculated. Their respective means were calculated over all of the poses for the corresponding strut data set. The deviation from the mean for each inter-target distance for every pose in the set was calculated. Poses where one or more of the distance deviations were greater than a threshold value were eliminated from the data set. The subset of acceptable data points was then fit to the equation of a sphere. Figure 5.8 shows a graph of the inter-target distances for strut 1 trial 1 before the rejection of bad data points. The horizontal lines are the limits set for the allowable deviation from the mean. For the SA-SB distances this limit is 0.018mm, and for the PR distances it is 0.013mm. Note the deviation in SA-SB which appears at poses 2, 19 and 20. Since the deviations from the mean are larger than the limits, these poses will be removed before the data is fit to a sphere.

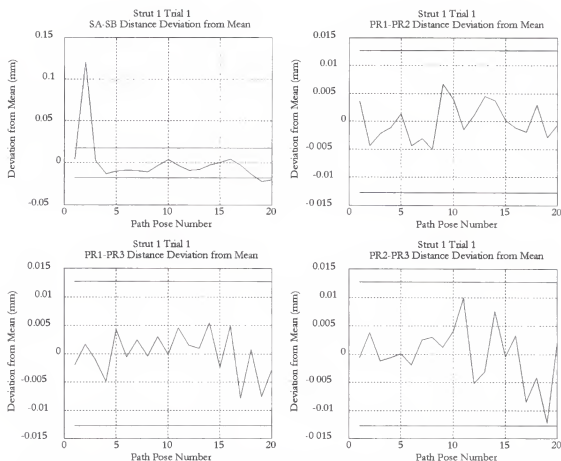


Figure 5.8 Inter-target distances Strut #1, Trial #1 before bad data point rejection

Figure 5.9 shows the results after the bad data points have been rejected. Notice all of the traces are within the acceptable inter-target mean deviation bound. The change in sphericity is noticeable from 0.024mm before bad data point removal, to 0.019mm after bad data point removal. The center location changed from (123.434, 351.072, 1292.556) to (123.432, 351.049, 1292.519). This method of bad data point rejection is used for all of the results reported in the rest of this work

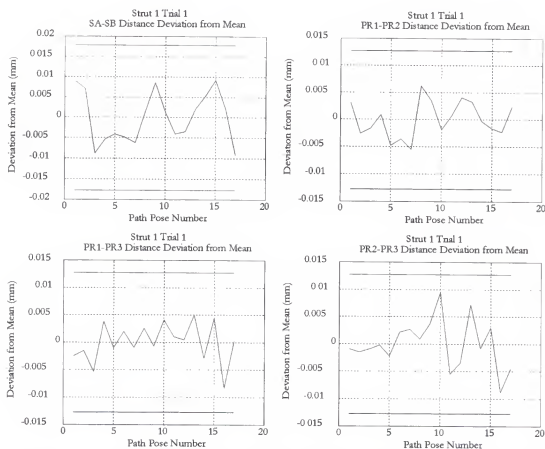


Figure 5.9 Inter-target distances for Strut #1, Trial #1 after bad data point rejection

5.2.3 Recovered Base Joint Locations

Table 5.1 shows the results for the base joint locations for all three trials using the filtered data point sets, plus the values provided in the original database. It should be noted that the results shown are referenced from the worktable top, which includes the results for the worktable location and orientation. "Total Data Points" refers to the number of data points used for the spherical fit after the rejection of bad data points. Table 5.2 shows the inter-base joint distances. By comparing the distances over the three trials and the original assumed nominal distances, it can be seen that the proposed method located the base joints correctly.

Table 5.1 Base joint location results for trials 1-3

Trial	Strut	X (mm)	Y (mm)	Z (mm)	R (mm)	Sphericity (mm)	Total Data Points
1	1	123.432	351.049	1292.519	412.901	0.0190	17
	2	408.542	-144.972	1292.796	434.870	0.0120	18
	3	285.984	-355.838	1293.249	410.970	0.0070	13
	4	-286.048	-354.743	1294.499	417.135	0.0180	16
	5	-407.419	-143.216	1294.304	404.265	0.0230	19
	6	-120.656	351.557	1293.139	438.343	0.0190	19
2	1	123.462	351.057	1292.543	391.221	0.0210	14
	2	408.558	-144.981	1292.754	450.811	0.0160	17
	3	286.069	-355.859	1293.235	449.121	0.0200	18
	4	-286.054	-354.746	1294.468	442.332	0.0250	20
	5	-407.450	-143.224	1294.330	453.137	0.0220	19
	6	-120.726	351.510	1293.134	430.027	0.0210	16
3	1	123.486	351.078	1292.451	429.259	0.0240	17
	2	408.560	-144.954	1292.742	419.701	0.0210	18
	3	286.074	-355.860	1293.333	467.007	0.0270	20
	4	-286.075	-354.807	1294.455	454.289	0.0240	16
	5	-407.450	-143.199	1294.252	449.598	0.0190	19
	6	-120.703	351.536	1293.123	435.269	0.0190	18
Orig.	1	121.847	353.309	1291.396	-	-	-
	2	408.005	-142.071	1291.500	-	-	-
	3	285.667	-353.347	1291.550	-	-	-
	4	-286.289	-353.168	1291.483	-	-	-
	5	-408.011	-142.071	1291.500	-	-	-
	6	-122.262	353.384	1291.500	-	-	-

Table 5.2 Distances between base joints for trials 1-3

Base Joint Pair	Trial 1 (mm)	Trial 2 (mm)	Trial 3 (mm)	Mean (mm)	Max-Min (mm)	Original (mm)
1-2	572.123	572.131	572.115	572.123	0.016	572.091
2-3	243.896	243.872	243.894	243.887	0.024	244.140
3-4	572.034	572.125	572.151	572.104	0.117	571.956
4-5	243.874	243.882	243.946	243.901	0.072	243.676
5-6	571.869	571.816	571.829	571.838	0.053	571.951
6-1	244.089	244.189	244.190	244.156	0.101	244.109

5.2.4 Recovered Platform Joint Locations

Table 5.3 shows the results for the platform joint locations for all three trials, plus the values in the original database. It should be noted that the results shown in Table 5.3 are referenced from the spindle nose, which includes the results for the spindle nose location and orientation.

The sphericity of the platform joint motion appears to be worse than that of the platform base joints. As explained in Chapter 4, this is due to the platform coordinate transformation which takes place at each measured platform pose. Since this transformation is calculated from the locations of the PR gage point for each pose, any measurement error propagates into the transformed strut gage point coordinates. In effect, each strut coordinate is not being transformed into a single PR system, but rather 20 PR systems which are very close to one another. The effect propagates through the transformed strut gage points, into the spherical fit, and shows up as nonshperical motion.

Table 5.3 Results for platform joint locations trials 1-3.

Trial	Strut	X (mm)	Y (mm)	Z (mm)	R (mm)	Sphericity (mm)	Total Data Points
1	1	149.860	86.865	306.988	387.054	0.019	17
	2	149.818	86.896	306.892	365.169	0.030	18
	3	0.816	-173.854	308.318	388.987	0.021	13
	4	0.909	-173.846	308.243	382.878	0.013	16
	5	-150.216	86.892	305.697	395.615	0.032	19
	6	-150.259	86.842	305.865	361.659	0.023	19
2	1	149.903	86.900	306.885	408.723	0.024	14
	2	149.869	86.881	306.835	349.088	0.024	17
	3	0.936	-173.884	308.242	350.743	0.017	18
	4	0.930	-173.864	308.240	357.529	0.029	20
	5	-150.229	86.876	305.569	346.816	0.034	19
	6	-150.262	86.786	305.672	370.038	0.025	16
3	1	149.881	86.893	306.882	370.625	0.022	17
	2	149.817	86.886	306.752	380.304	0.021	18
	3	0.838	-173.850	308.223	332.972	0.030	20
	4	0.875	-173.811	308.115	345.691	0.031	16
	5	-150.357	86.883	305.738	350.058	0.038	19
	6	-150.273	86.907	305.724	364.713	0.025	18
Orig.	1-2	150.219	86.760	306.547	-	-	-
	3-4	1.203	-173.892	308.188	-	-	-
	5-6	-149.827	86.760	305.785	-	-	-

Table 5.4 shows the inter-platform joint distances computed from the best-fit centers. Strut pairs 1/2, 3/4, and 5/6 share platform joint locations through the bifurcated ball joint. Therefore, it is expected when the distances between the recovered joint centers are calculated, there will be zero distance between the supposedly coincident platform joint centers. This however is not the case. Table 5.4 shows that these shared joint locations have some small distance between them.

There are two possible explanations for this. The first is numerical conditioning of the strut gage point data. In Chapter 4, it was shown that small amounts of measurement and

machine positioning uncertainty, translated into large recovered joint center uncertainties. It is possible that even though the joint centers actually are coincident, they do not appear to be exactly coincident due to the measurement error.

Table 5.4 Distances between platform joints trials 1-3.

Platform Joint Pair	Trial 1 (mm)	Trial 2 (mm)	Trial 3 (mm)	Mean (mm)	Max-Min (mm)	Original (mm)
1-2	0.109	0.063	0.145	0.106	0.082	0.000
2-3	300.323	300.302	300.300	300.309	0.023	300.246
3-4	0.120	0.021	0.121	0.087	0.100	0.000
4-5	301.379	301.399	301.394	301.391	0.020	301.256
5-6	0.180	0.141	0.088	0.137	0.092	0.000
6-1	300.121	300.167	300.156	300.148	0.046	300.047

The second possibility is that the joint centers truly are not coincident. One strut rides on a bearing which is supposed to be located at the center of the solid sphere part of the bi-ball joint. If this axle does not pass through the sphere center, the axle will precess around the center of the joint as the solid sphere rotates in the magnetic cup. This motion will introduce a strut length error which is seen by the platform PR system, and hence introduced into the strut gage point measurement when the coordinates are translated into the PR system.

5.3 Results: Determining the Initial Lengths

Once the platform and base joint locations were calculated, the initial strut lengths were calculated. The process of homing the machine and measuring the PR gage point locations was repeated 20 times. From these gage point locations, the location of the platform joint centers were calculated relative to the M system, and the distances between cor-

responding joint centers were determined. Figure 5.10 shows the deviation of the PR inter-target distances during the measuring sequence. The deviations between the target locations were well inside the limits of ± 0.013 mm. This was a typical result for all three trials.

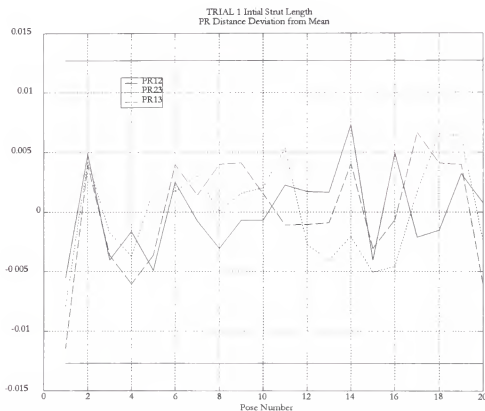


Figure 5.10 Trial #1 PR inter-target distances during initial strut length data collection.

In every trial, all 20 locations were considered acceptable by this criteria. Therefore, all 20 poses were used in each trail to calculate the mean initial strut lengths. Table 5.5 shows the calculated initial strut lengths for each trial, plus the values from the original database. Notice the lengths are not exactly the same for each trial. This does not come as a surprise. Since the initial lengths are calculated from the joint locations, any deviation in the joint locations will cause deviations in the calculated initial strut lengths. Moreover, the influence of measurement error in the PR gage points described previously also contributes to these deviations.

Table 5.5 Results for initial strut lengths trials 1-3.

Strut	Trial 1 (mm)	Trial 2 (mm)	Trial 3 (mm)	Original (mm)
1	456.708	456.657	456.567	456.654
2	455.324	455.198	455.282	460.297
3	455.428	455.370	455.470	455.489
4	454.211	454.096	454.239	459.225
5	457.072	457.135	456.969	457.287
6	459.985	460.006	459.928	460.009

5.4 Results: Strut Extension Mapping

5.4.1 Trial 1

The struts were commanded to extend by 23.25mm for a total of 20 poses. Figure 5.11 shows that there were no poses considered to have bad data points.

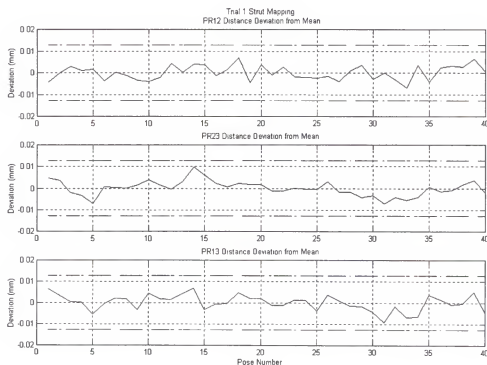


Figure 5.11 Trial #1 PR inter-target distance deviations during strut extension mapping.

Figures 5.12a-f show the results of the strut extension error mapping for all six struts for trial 1. When determining the axis positioning error in a linear guideway, there is usually a strong linear trend in the graphs of both the forward (solid line) and reverse (dotted line) paths. The reverse path graph should have the same slope as the forward, but offset above the forward path. This offset is reversal error due to backlash occurring between the screw and the nut (in screw driven systems). The paths in Figure 5-15 show a general linear trend, but are very jagged and do not correspond with the typical expected results for error in a linear guideway. The spacing of 23.25mm however is very coarse. A more finely spaced mapping may show the trends more accurately.

5.4.2 Trial 2

Trial 2 was a much more dense sampling of the strut extension. A platform pose was recorded every 3mm of strut extension length for a total of 300 poses (150 extension, 150 retraction) or 450mm of strut extension length. Figure 5.13 is a plot of the PR inter-target distances. The horizontal dotted lines represent the threshold value for data rejection (0.013mm). With the exception of only a very few poses, the inter-target distances repeat very well. All poses were considered acceptable, and none were thrown out. Figures 5.14a-f show the results of the strut extension mapping for trial 2. Looking at the graphs for struts 1 and 6 there is a large jump occurring at about 1/3 from the end. This is not believed to be an actual motion produced by the machine. These jumps are related to the way the extension data was collected. Due to the length of time required to collect all 300 poses (900 measurements total) the data was broken up into six smaller files, reducing the likelihood that a single experimental error in the data collection would ruin the entire experiment.

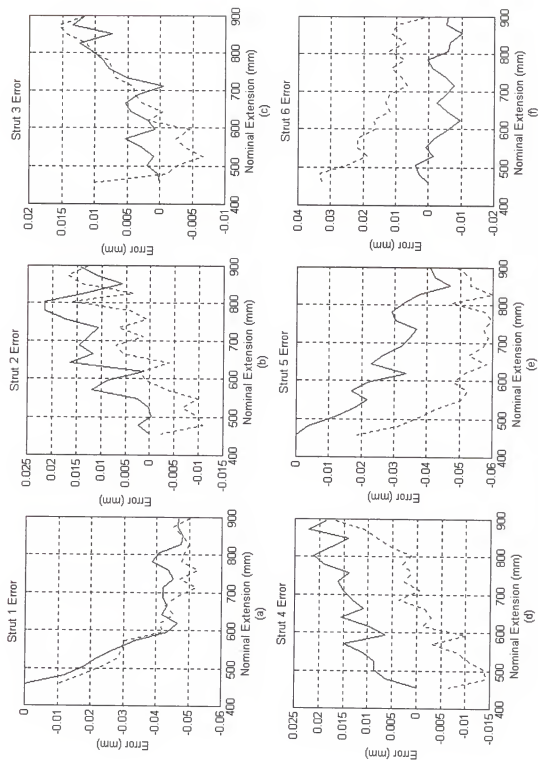


Figure 5.12 Trial #1 strut extension mapping, strut: (a) 1, (b) 2, (c) 3, (d) 4, (e) 5, (f) 6.

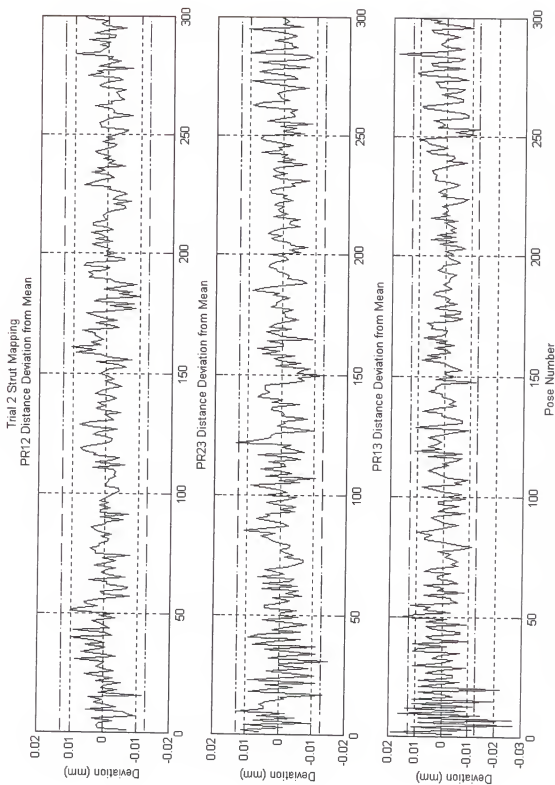


Figure 5.13 Trial #2 PR inter-target distance deviations during strut extension mapping.

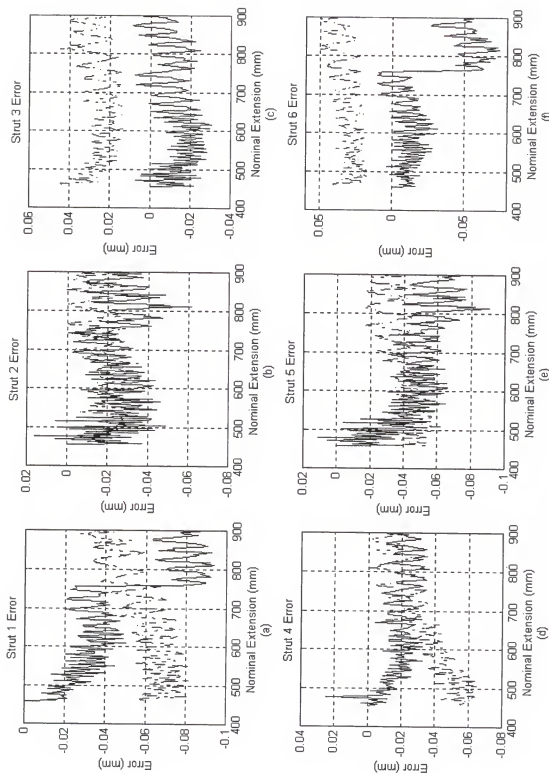


Figure 5.14 Trial #2 strut extension mapping, strut: (a) 1, (b) 2, (c) 3, (d) 4, (e) 5, (f) 6.

At the beginning of each file the location of the R system relative to the tracker was recorded. In case the tracker was moved in between the measurement sets, correct measurements could still be recorded. This method should have prevented the jumps shown in the graphs for struts 1 and 6. However, if these jumps are related to an incorrect reading of the R system it would be expected that this jump would show up in all six graphs not just two. What makes this more interesting is the fact that struts 1 and 6 are joined together at the same platform joint. The origin of this discrepancy cannot be definitively answered except that it must be an experimental measurement error.

The denser sampling also revealed an unexpected periodic motion in the strut extension which appears to have a higher frequency when the struts are shorter than when they are longer.

5.4.3 Trial 3

After reviewing the strut extension mapping for trial 2, and considering the amount of time it took to collect the data, it was decided that these results were sufficient. Since the setup of the fixtures was not disturbed between trials 2 and 3, data in each set is interchangeable with that of the other. Therefore it was decided to use the strut extension mapping for trial 2 with the rest of the collected data from trial 3. Since the same data set was used for extension mapping between trials 2 and 3, the acceptable data points are exactly the same as in trial 2.

5.5 Results: Dynamic Renishaw Ball Bar Tests

Each of the three new kinematic parameter databases, as well as the original, were loaded into the machine controller. For each database the machine then was run through a

series of six different dynamic ball bar tests for a total of 24 tests. It should be stated at this time that the strut extension lookup tables were not implemented, due to the fact that the version of the control software (v3.9) which the machine was running at the time was not capable of interpreting strut extension lookup tables. Table 5.6 shows a compiled list of all of the results for each database over the 24 tests using the recovered joint locations and initial strut lengths.

Table 5.6 Results of dynamic Renishaw ball bar tests.

Database	Circle Number	Radial Deviation		Best-Fit Radius mm	Center Position	
		Max μm	Min μm		X μm	Y μm
Original	1	32.2	-30.6	149.987	-7.2	-37.2
	2	27.5	-26.1	150.010	-32.6	-41.2
	3	61.1	-71.2	149.996	14.4	-21.1
	4	42.9	-37.1	149.965	-11.5	-5.5
	5	57.1	-56.2	149.987	-34.9	-21.1
	6	68.8	-61.3	299.996	1.0	-15.1
Trial 1	1	20.3	-20.1	149.978	-17.8	-39.9
	2	20.0	-27.1	149.990	-21.3	-25.9
	3	33.3	-40.5	149.986	3.7	-21.8
	4	45.5	-41.0	149.961	-18.1	-20.1
	5	46.5	-43.4	149.977	-10.9	-14.8
	6	41.3	-41.0	299.973	18.8	-9.5
Trial 2	1	24.6	-26.6	149.998	-36.9	-26.6
	2	36.5	-42.0	149.994	-50.9	-15.0
	3	46.6	-50.6	150.005	-5.0	-11.8
	4	35.8	-30.5	149.995	-6.5	4.8
	5	46.9	-35.9	149.994	-9.3	6.4
	6	59.0	-61.2	300.007	-8.7	-17.7
Trial 3	1	27.2	-31.6	149.996	13.8	-24.5
	2	22.6	-29.1	150.012	-14.4	-14.5
	3	19.5	-24.6	150.003	18.0	-16.6
	4	53.2	-63.3	149.982	-13.6	-23.2
	5	52.9	-56.9	150.003	-11.1	-0.9
	6	48.6	-56.5	300.022	18.1	-27.5

It is difficult by merely looking at the numbers in the table to determine whether the determination of the kinematic parameters was successful. A metric is needed which takes into account the radial deviation and the center location of the best-fit circle, in order to make a direct comparison. Since it is possible to have a circle which is centered at (0,0), but have a large radial motion error component, the metric must reflect both the circularity of the trace and the distance of the center of the trace from the origin. The following quality index was adopted.

$$\text{Quality Index (mm)} = \frac{\text{Radial Deviation}_{\max} - \text{Radial Deviation}_{\min} + \sqrt{x_{\text{center}}^2 + y_{\text{center}}^2}}{1000}$$

The quality index for penalizes both non-circular motion and center location of the best fit circle. The smaller the number (zero being the best), the better the test results. Using this definition, the quality indices, the quality index range (max-min) and the means of the quality indices are calculated (Table 5.7). It is desirable for the range of the quality index to be as low as possible. This means there is little variation in the performance of the machine from workspace location to workspace location. Also it is important that the mean be as small as possible. The lower the mean, the better the overall performance of the machine in different workspace locations. From Table 5.7 it can be seen that of all four databases available, trial #1 had the best overall performance.

Table 5.7 Ball bar contour quality index

Circle	Original	Trial 1	Trial 2	Trial 3
1	0.101	0.084	0.097	0.087
2	0.106	0.081	0.132	0.072
3	0.158	0.096	0.110	0.069
4	0.093	0.114	0.074	0.143
5	0.154	0.108	0.094	0.121
6	0.145	0.103	0.140	0.138
Range	0.065	0.033	0.066	0.075
Mean	0.126	0.098	0.108	0.105

CHAPTER 6 CONCLUSIONS AND FUTURE WORK

6.1 Conclusion

This research started out with three goals. The first goal was to create a new method to determine all of the kinematic parameters in a fully assembled Stewart platform kinematic parallel mechanism. The second was to create a method for determining the uncertainty in the recovered kinematic parameters, and the propagation of these uncertainties through the mechanism to the tool tip, which was to be applied to a real-world situation. The third goal was to calibrate a machine in the field using the proposed method. All of these goals were met.

6.1.1 Summary of Proposed Method

The method proposed has five steps: locating the worktable, locating the joint centers, locating the spindle relative to the platform joints, determination of the initial strut lengths, and mapping the extension lengths of all six actuators simultaneously. Although this method was only tested on one type of a Stewart platform device (6-3), there are no machine specific limitations which would prevent the method from being adapted to other fully assembled Stewart platform devices and may possibly be used to calibrate other kinematic parallel devices not based on Stewart platforms. A secondary goal of the method development was to not use any precision artifacts which were expressly designed to be used during calibration. Although some fixtures were designed and fabricated which

were used to mount the gage points to the machine, the fixtures were inexpensive and were not considered to be precision artifacts such as ring gages or ballplates.

6.1.2 Summary of Uncertainty Analysis

A method for determining the uncertainty in each of the kinematic parameters was developed and performed based on the real-world problem of calibrating a Hexel Tornado 2000 milling machine in the field using an SMX laser tracker. Based upon the tool paths used and assuming uncertainty scenario #4 was the most realistic case for the machine and measuring instrument chosen, the base joint locations may be resolved to approximately 0.07mm from their true positions. Platform joint centers may be resolved to approximately 0.1mm from their true positions. Initial strut lengths may be resolved to approximately 0.07mm. Measurement uncertainty had the largest impact on the degradation of the simulation results. CED was cut by nearly 1/3 and initial strut length uncertainty was cut by nearly 1/2 by eliminating the measurement uncertainty. This is due mainly to the fact that several coordinate reference frames are repeatedly measured during the experimental procedure. The uncertainty and error in the location and orientation of these measured coordinate reference frames propagates directly into the kinematic parameters over and over again. Results from the calibration Monte Carlo simulations that it would appear that the measuring instrument should be as accurate as possible with the least uncertainty. However, strut length uncertainty should not be overlooked or discounted even if a very accurate measuring instrument were to be used.

The uncertainty analysis does show that the method is reasonably good at determining the locations of the joint centers and the initial lengths (when used with an appropriate measuring device). However, due to the accumulation of uncertainties it does not appear

to provide a good way for determining the strut extension variation.

Results from the simulated circular paths for the four uncertainty scenarios indicate that strut length uncertainty is very damaging to the machine's contouring performance. In fact it appears to be much more detrimental than joint location uncertainty. This is due to the fact that strut length uncertainty directly affects the uncertainty in the location of the platform and hence the tool point location. Joint center location uncertainty is projected into the strut lines of action, so only a small amount of the possibly large joint location uncertainty affects the platform location. So it can be concluded that the best way to improve the performance of a Stewart platform machine is to first cut down the amount of error occurring in the strut length through better strut design, direct sensing of the strut lengths, and elimination of errors projected into the strut lines of action from the joints. The second way to improve the performance of a Stewart platform machine once the strut lengths may be found accurately is to precisely locate the joint centers relative to the worktable or to the spindle nose (base and platform joints respectively).

6.1.3 Summary of Experimental Results

The method was performed a total of three times on a Hexel Tornado 2000 milling machine using a SMX laser tracker. Each trial took two-eight hour days for one person to collect the data needed to determine the joint locations, spindle location and the initial lengths. Another eight hour day was needed to collect the data for the 3mm density screw extension error mapping. This meets the goal originally set of 2-3 business days. Methods to reject bad data points also had to be created to remove suspect data from the measurements. All of the kinematic parameters were successfully recovered in all three trials. Three new machine databases were created out of these three sets of kinematic parameters

and were implemented in the Hexel's controller. Dynamic Renishaw ball bar circles were performed in six locations with two radii (150mm and 300mm) to determine the difference in machine performance between the three new parameter sets and the original parameter set. Although the method did appear to determine the correct kinematic parameters, there was no obvious, overwhelming improvement in the positioning performance of the Hexel, however it does not appear that the positioning performance was worsened either. The performance of the calibrated machine appears to be predicted best by uncertainty scenario #4.

Given the amount of preplanning and calculation required, the somewhat time consuming data collection, and the need for a high precision (implying expensive) spatial coordinate measuring device required to collect the data, this method with some fine tuning still is a viable technique to calibrate fully assembled Stewart platform machines in the field. Although these may seem to be shortcomings of this method, they are merely difficulties which may mostly be solved or avoided altogether with good computer programming and the next generation of spatial coordinate measuring devices, and do not appear to be major flaws which would make this method undesirable or impractical.

6.2 Future Work

6.2.1 Kinematic Parameter Sensitivity Analysis

In light of the results for the uncertainty analysis, more work should be done on determining the effect of uncertainties in individual kinematic parameters on the overall volumetric performance of the PKMs in general. From the results in Chapter 4, it appears that

a lot can be learned about design improvements and design criterion for particular machine designs from a rigorous sensitivity analysis.

6.2.2 Effects of Spherical Data Point Distribution

The effects of data point distribution on the surface of spheres were not research at all in this effort. It is entirely possible that more data points spread over the largest surface of the sphere as possible will improve the accuracy in joint location part of this method. An effort should be made to determine the effect of the number and distribution of the data point over the surface of the spheres on the accuracy of the joint location recovery method. This also may be expanded to determine the locations of the least number of data points required to accurately determine the joint center locations given the uncertainties in the machine and the measurement apparatus. Also a more accurate uncertainty simulation which uses error models of both the machine to be calibrated and the measuring device may be of some use.

Improved methods in determining the best data collection sites more than likely will lead to the software automation of selecting the path points which would include the creation of the M/G code file necessary to direct the machine to follow the desired path. This would eliminate the need to guess at which collection sites should be used, and would greatly reduce the time required to select the collection sites and create the necessary path programs.

6.2.3 Explore Related Fixed-Strut Calibration Methods

The proposed method also may be able to be applied in different forms. The idea proposed in this work of holding one strut fixed was explored. It may be possible to create

methods building on this technique which hold two or more struts fixed which may potentially yield even better results and be easier to execute.

6.2.4 Explore Invention of Affordable Six DOF Measuring Devices

An area not directly related to this method itself but nonetheless very useful and would certainly make the data collection easier would be the creation of a six DOF measuring device. A number of gage points were needed in this method to determine the six degrees of freedom necessary to uniquely define coordinate reference frames in space. It would be very useful to have a device that did this in one step, which would greatly reduce the data collection time.

APPENDIX A COORDINATE TRANSFORMATIONS

A.1 Homogeneous Coordinates

The homogeneous form of coordinates is essentially a four dimensional method of expressing three dimensional Cartesian coordinates. Homogeneous coordinates are the Cartesian coordinates of a point (x,y,z) divided by a scaling factor “w”.

$$q = \begin{bmatrix} x/w \\ y/w \\ z/w \\ w \end{bmatrix}$$

The scaling factor “w” does have special and significant uses, but will not be discussed in this work. Since the manipulation of the Cartesian coordinates of points between different coordinate systems is of the most interest in this body of work, “w” will always be taken to equal 1.

A.1.1 Single Point Notation

The homogeneous coordinates of a single point is denoted by a lowercase letter indicating the point, with a leading superscript indicating the reference frame. For example the point “q” as measured in the “W” system would be:

$${}^W q = \begin{bmatrix} ({}^W q)_x \\ ({}^W q)_y \\ ({}^W q)_z \\ 1 \end{bmatrix}$$

A.1.2 Ordered Matrix of Homogeneous Coordinates

The homogeneous coordinates of several points expressed in the same coordinate system may appear in an ordered matrix. Matrices of homogeneous point coordinate are denoted by the corresponding uppercase letter. A particular point contained in the matrix is referenced by a numerical subscript. A matrix of three different coordinates q_1 , q_2 , and q_3 , referenced in the “W” system would be:

$${}^W Q = \begin{bmatrix} {}^W q_1 & {}^W q_2 & {}^W q_3 \end{bmatrix} = \begin{bmatrix} {}^W x_{q_1} & {}^W x_{q_2} & {}^W x_{q_3} \\ {}^W y_{q_1} & {}^W y_{q_2} & {}^W y_{q_3} \\ {}^W z_{q_1} & {}^W z_{q_2} & {}^W z_{q_3} \\ 1 & 1 & 1 \end{bmatrix}$$

A.2 Homogeneous Coordinate Transformations

The transformation of the coordinates of points from one system to another is performed by a homogeneous coordinate transformation (HTM) matrix. An HTM is a 4x4 matrix which mathematically describes the position and rotation of one coordinate system relative to another.

A.2.1 HTM Notation

The notation for an HTM as used in this paper is a pre-superscripted and post-subscripted “T”. The superscripted letter refers to the system to which the coordinates are transformed. The subscripted letter refers to the coordinate system from which the coordinates are transformed. The corresponding notation for an HTM describing the transformation from a system “B” to a system “A” would be ${}^A T_B$. This notation can also be read as

“the B system expressed in the A”, “the B system as seen in the A”, or even shorter “the B in the A.”

A.2.2 HTM Construction

An HTM is constructed from two parts - a rotation matrix R, and an origin vector P_0 .

$${}^A T_B = \begin{bmatrix} [{}^A R_B]_{3 \times 3} & \{{}^A P_{Bo}\}_{3 \times 1} \\ 0 & 0 & 0 & 1 \end{bmatrix}_{4 \times 4}$$

For orthogonal Cartesian (X,Y,Z) coordinate systems, the “R” matrix is an orthonormal 3x3 matrix whose columns are the orthogonal unit vectors of the current system “B” as seen in the new system “A”.

$$\begin{aligned} {}^A R_B &= \begin{bmatrix} {}^A(\hat{x})_B & {}^A(\hat{y})_B & {}^A(\hat{z})_B \end{bmatrix} \\ &= \begin{bmatrix} {}^A(\hat{x}_x)_B & {}^A(\hat{y}_x)_B & {}^A(\hat{z}_x)_B \\ {}^A(\hat{x}_y)_B & {}^A(\hat{y}_y)_B & {}^A(\hat{z}_y)_B \\ {}^A(\hat{x}_z)_B & {}^A(\hat{y}_z)_B & {}^A(\hat{z}_z)_B \end{bmatrix} \end{aligned}$$

The origin position vector “P” is the (x,y,z) position of the current system “B” as seen from the new system “A”.

$$\{{}^A P_{Bo}\} = \begin{Bmatrix} ({}^A P_{Bo})_x \\ ({}^A P_{Bo})_y \\ ({}^A P_{Bo})_z \end{Bmatrix}$$

A.2.3 HTM Construction from Three Points

An HTM relating an existing system “A” to a new system “B” defined by three points

Aq_1 , Aq_2 , and Aq_3 may be constructed using the formula:

$${}^AT_B = \begin{bmatrix} {}^Ax_B & {}^Ay_B & {}^Az_B & {}^Aq_1 \\ 0 & 0 & 0 & 1 \end{bmatrix}$$

$${}^Ax_B = \frac{{}^Aq_2 - {}^Aq_1}{{}^Aq_2 - {}^Aq_1} \quad {}^Az_B = {}^Ax_B \times \frac{{}^Aq_3 - {}^Aq_1}{{}^Aq_3 - {}^Aq_1} \quad {}^Ay_B = {}^Az_B \times {}^Ax_B$$

A.2.4 Rotation matrix construction from a vector (n) and a rotation (θ)

Given a vector $\underline{n} = (n_x, n_y, n_z)$ and a desired rotation about the vector (θ), the 3x3 rotation matrix may be calculated

$${}^AR_B = \begin{bmatrix} n_x n_x v + c & n_x n_y v - n_z s & n_x n_z v + n_y s \\ n_x n_y v + n_z s & n_y n_y v + c & n_y n_z v - n_x s \\ n_x n_z v - n_y s & n_y n_z v + n_x s & n_z n_z v + c \end{bmatrix}$$

$$c = \cos(\theta) \quad s = \sin(\theta) \quad v = 1 - \cos(\theta)$$

A.2.5 Inverse of an HTM

The matrix inverse of an HTM has the special construction:

$${}^BT_A = ({}^AT_B)^{-1} = \begin{bmatrix} [{}^AR_B]^T & -[{}^AR_B]^T \{ {}^AP_{Bo} \} \\ 0 & 0 & 0 & 1 \end{bmatrix}$$

A.2.6 HTM Usage

Once the proper HTM's have been constructed relating coordinate system pairs, it is possible to use the HTM's to transform coordinates expressed in one system to another.

If four coordinate systems A, B, C, and D exist, and the HTM's ${}^A T_B$, ${}^D T_B$, and ${}^D T_C$ are known then we can express the coordinates of a point ${}^A q$ in the C system.

$$\begin{aligned} {}^C q &= {}^C T_D \cdot {}^D T_B \cdot {}^B T_A \cdot {}^A q \\ &= ({}^D T_C)^{-1} \cdot {}^D T_B \cdot ({}^A T_B)^{-1} \cdot {}^A q \end{aligned}$$

APPENDIX B FITTING DATA TO BASIC GEOMETRIC OBJECTS

This appendix contains the derivation of least squares closed-form solutions for best-fit spheres, planar circles, planes, skew circles and three-dimensional lines for a given set of experimentally determined data.

B.1 Least Squares Method

The least squares method gets its name from the mathematical definition of the problem itself, where the values of a set of unknown parameters “x” are determined by finding the minimum of the square of a reference residual function “f(x)” over a set of n observations “p”.

$$\text{Minimize } \sum_{i=1}^n f_i^2(x, p_i)$$

The residual equation f has the general form:

$$f_i(x, p_i) = g_{\text{nominal}}(x, p_i) - g_{\text{experimental}}(x, p_i) \quad i=1 \text{ to } n$$

From calculus, the minimum of a multivariate function occurs when the total derivative of the function with respect to its arguments is equal to zero.

$$\frac{df}{dx} = \frac{\partial f}{\partial x_1} dx_1 + \frac{\partial f}{\partial x_2} dx_2 + \dots + \frac{\partial f}{\partial x_n} dx_n = 0$$

B.2 Calculating the Best-Fit Sphere

The least squares method can be used to formulate a closed-form solution for calculating the center coordinates (h,k,l) and radius "r" of the best-fit sphere for a given set of n three-dimensional Cartesian coordinates (x,y,z).

The square of the distance " r_i " from the i^{th} data point to the best fit sphere center (h, k, l) may be calculated by the equation:

$$r_i^2(h, k, l) = (x_i - h)^2 + (y_i - k)^2 + (z_i - l)^2 \quad i=1 \text{ to } n$$

The equation of the residual, which is in this case the difference between the square of the best-fit sphere radius and the distance r_i , may be determined by the equation:

$$f_i(h, k, l, r) = r^2 - r_i^2 = r^2 - (x_i - h)^2 - (y_i - k)^2 - (z_i - l)^2 \quad i=1 \text{ to } n$$

Expanding the equation f_i :

$$f_i(h, k, l, r) = 2x_i h + 2y_i k + 2z_i l + C - (x_i^2 + y_i^2 + z_i^2) \quad i=1 \text{ to } n$$

$$f_i(x) = \begin{bmatrix} x_i & y_i & z_i & 1 \end{bmatrix} \cdot \begin{bmatrix} 2h \\ 2k \\ 2l \\ C \end{bmatrix} - (x_i^2 + y_i^2 + z_i^2) \quad i=1 \text{ to } n$$

$$\text{where} \quad C = r^2 - h^2 - k^2 - l^2$$

Considering all n data points, f can be written as a set of linear equations:

$$f(\underline{x}) = \begin{bmatrix} x_1 & y_1 & z_1 & 1 \\ x_i & y_i & z_i & 1 \\ x_m & y_m & z_m & 1 \end{bmatrix} \cdot \begin{bmatrix} 2h \\ 2k \\ 2l \\ C \end{bmatrix} - \begin{bmatrix} x_1^2 + y_1^2 + z_1^2 \\ x_i^2 + y_i^2 + z_i^2 \\ x_m^2 + y_m^2 + z_m^2 \end{bmatrix} = A \cdot \underline{x} - \underline{b}$$

Setting the derivative of $f^2(\underline{x})$ to zero, the unknown vector \underline{x} may be uniquely determined:

$$\begin{aligned}
 \frac{d}{d\underline{x}}(f^T \cdot f) &= 0 \\
 \frac{d}{d\underline{x}}(A \cdot \underline{x} - \underline{b})^T \cdot (A \cdot \underline{x} - \underline{b}) &= 0 \\
 \frac{d}{d\underline{x}}(\underline{x}^T A^T A \underline{x} - \underline{x}^T A^T \underline{b} - \underline{b}^T A \underline{x} + \underline{b}^T \underline{b}) &= 0 \\
 \frac{d}{d\underline{x}}(\underline{x}^T A^T A \underline{x} - 2\underline{x}^T A^T \underline{b} + \underline{b}^T \underline{b}) &= 0 \\
 d\underline{x}^T A^T A \underline{x} - d\underline{x}^T A^T \underline{b} &= 0 \\
 d\underline{x}^T (A^T A \underline{x} - A^T \underline{b}) &= 0 \\
 A^T A \underline{x} - A^T \underline{b} &= \underline{0} \\
 \underline{x} &= (A^T A)^{-1} A^T \underline{b}
 \end{aligned}$$

Assuming the data set is well conditioned, meaning $A^T A$ is not singular or close to being singular, the center coordinates (h,k,l) and radius for the best fit sphere may be calculated from the expressions:

$$h = \frac{-x_1}{2} \quad k = \frac{-x_2}{2} \quad l = \frac{-x_3}{2} \quad r = \sqrt{x_4 + h^2 + k^2 + l^2}$$

B.3 Calculating the Best-Fit Circle

With one less DOF than the solution for the sphere, the equation for the residual “f” for the best-fit circle is

$$f(\underline{x}) = \begin{bmatrix} x_1 & y_1 & 1 \\ x_i & y_i & 1 \\ x_m & y_m & 1 \end{bmatrix} \cdot \begin{bmatrix} 2h \\ 2k \\ C \end{bmatrix} - \begin{bmatrix} x_1^2 + y_1^2 \\ x_i^2 + y_i^2 \\ x_m^2 + y_m^2 \end{bmatrix} = A \cdot \underline{x} - \underline{b}$$

where $C = r^2 - h^2 - k^2$

Using the general solution for a residual in the form:

$$f = A \cdot x - b$$

the values for h, k and r for the best-fit circle may be determined by the expressions:

$$h = \frac{-x_1}{2} \quad k = \frac{-x_2}{2} \quad r = \sqrt{x_3 + h^2 + k^2}$$

B.4 Calculating the Best-Fit Plane

The least squares method may be used to formulate a closed-form solution for calculating the normal vector “n” and the distance D from the origin of the best-fit plane for a given set of n three-dimensional Cartesian coordinates.

For the i^{th} data point, the distance D_i between the point and the plane is

$$D_i(n) = \begin{bmatrix} x_i & y_i & z_i \end{bmatrix} \cdot n = x_i n_x + y_i n_y + z_i n_z \quad i=1 \text{ to } n$$

The equation of the residual for the i^{th} data point then becomes

$$f_i(n, D) = D - D_i = D - (x_i n_x + y_i n_y + z_i n_z) \quad i=1 \text{ to } n$$

Rearranging f into matrix format:

$$f(x) = \begin{bmatrix} x_1 & y_1 & z_1 \\ x_i & y_i & z_i \\ x_n & y_n & z_n \end{bmatrix} \cdot \begin{bmatrix} -n_x \\ -n_y \\ -n_z \\ D \end{bmatrix} = A \cdot x$$

Applying the least squares criteria:

$$\begin{aligned}\frac{d}{d\mathbf{x}}(f^T \cdot f) &= 0 \\ \frac{d}{d\mathbf{x}}(A \cdot \mathbf{x})^T \cdot (A \cdot \mathbf{x}) &= 0 \\ \frac{d}{d\mathbf{x}}(\mathbf{x}^T A^T A \mathbf{x}) &= 0 \\ \frac{d\mathbf{x}}{d\mathbf{x}}^T (A^T A \mathbf{x}) &= 0 \\ A^T A \mathbf{x} &= 0\end{aligned}$$

Thinking of this equation in terms of an eigenvalue problem ($A^T A \mathbf{x} = \lambda \mathbf{x}$), it stands to reason that the eigenvector $\mathbf{x}_{\lambda=0}$ corresponding to the eigenvalue $\lambda=0$ of the $A^T A$ matrix would be the solution to the problem. The values for the unit normal and the offset distance D of the plane may then be calculated:

$$\begin{aligned}n &= \frac{-((X_{\lambda=0})_1, (X_{\lambda=0})_2, (X_{\lambda=0})_3)}{\sqrt{(X_{\lambda=0})_1^2 + (X_{\lambda=0})_2^2 + (X_{\lambda=0})_3^2}} \\ D &= \frac{(X_{\lambda=0})_4}{\sqrt{(X_{\lambda=0})_1^2 + (X_{\lambda=0})_2^2 + (X_{\lambda=0})_3^2}}\end{aligned}$$

B.5 Calculating the Best-Fit Skew Circle

Calculating the best-fit skew circle for a set of n three-dimensional data points is done by using combination of the plane and circle fitting algorithms which have already been derived.

The solutions for the surface normal and offset distance of the best-fit plane are found first. The current coordinate system is rotated such that the Z -unit vector is rotated to be parallel to the direction of the plane's surface normal, and then translated along the new Z -

axis by the offset distance to the plane. The coordinates of the data points are then transformed into the new coordinate system and projected on to the XY plane which is now coincident with the best-fit plane. Using the circle fitting algorithm, the best-fit circle for the data projected into the XY plane may be determined. Using the inverse coordinate transformation, the location of the center and the radius of the best-fit circle may be transformed back to the original coordinate system.

B.6 Calculating the Best-Fit Line

The least squares method can be used to formulate a closed-form solution for parametric equations as well. The parametric equations in “t” of the coordinates (X,Y,Z) on a three-dimensional line:

$$X(t) = m_x t + b_x$$

$$Y(t) = m_y t + b_y$$

$$Z(t) = m_z t + b_z$$

The data fitting problem to be solved is given a set of n of experimentally collected coordinates (x,y,z), determine the Plucker line coordinates {S;S₀} of the best-fit line, where “S” is the line’s unit vector, and “S₀” is the line’s moment about the origin. This is done by applying the least squares method to each of the equations X(t), Y(t) and Z(t). Since the application is exactly the same for each equation, only the derivation for the X(t) equation will be shown here.

Using the equation for X(t), the residual “f_i” of the ith measurement is

$$f_i = X(i) - x_i = m_x i + b_x - x_i \quad i=1 \text{ to } n$$

Writing all f_i as a set of linear equations, the equation for f becomes

$$f = \begin{bmatrix} 1 & 1 \\ i & 1 \\ n & 1 \end{bmatrix} \cdot \begin{bmatrix} m_x \\ b_x \end{bmatrix} - \begin{bmatrix} x_1 \\ x_i \\ x_n \end{bmatrix} = A \cdot x - \underline{b}$$

Using the general solution for a residual in the form:

$$f_i = A \cdot x - \underline{b}$$

the answer can simply be written down:

$$\begin{bmatrix} m_x \\ b_x \end{bmatrix} = \left(\begin{bmatrix} 1 & i & n \\ 1 & 1 & 1 \\ n & 1 & \end{bmatrix} \begin{bmatrix} 1 & 1 \\ i & 1 \\ n & 1 \end{bmatrix} \right)^{-1} \begin{bmatrix} 1 & i & n \\ 1 & 1 & 1 \\ n & 1 & \end{bmatrix} \begin{bmatrix} x_1 \\ x_i \\ x_n \end{bmatrix}$$

This is done for the $Y(t)$ and $Z(t)$ equations as well to yield the rates of change of X , Y , and Z with respect to t (m_x , m_y , m_z) and the offsets (b_x , b_y , b_z). The rates of change when placed in a vector and unitized forms the unit vector S of the best fit line.

$$\underline{S} = \frac{(m_x, m_y, m_z)}{\sqrt{m_x^2 + m_y^2 + m_z^2}}$$

The moment S_0 of the line is calculated by

$$S_0 = (b_x, b_y, b_z) \times S$$

APPENDIX C STEWART PLATFORM KINEMATICS

C.1 Instantaneous Kinematics

C.1.1 Construction of Jacobian

The Jacobian of a manipulator is a matrix which maps small motions or velocities occurring at the tool point into small joint motions or velocities given a nominal pose of the mechanism. In order to construct the Jacobian of a Stewart platform, the locations of the base (B) and platform (P) joints must be known relative to a single system. For the purposes of example, the tool tip (Tl) frame will be used (^{Tl}B, ^{Tl}P respectively see Chapter 1 and Appendix A).

The simplest way to construct the Jacobian is by calculating the Plucker line coordinates for each joint in the mechanism and arranging them in a matrix. The six Plucker line coordinates ^{Tl}(S;₀)_i for a line connecting point ^{Tl}P_i to ^{Tl}B_i are may be computed by

$$l_i^2 = ((^{Tl}B_x)_i - (^{Tl}P_x)_i)^2 + ((^{Tl}B_y)_i - (^{Tl}P_y)_i)^2 + ((^{Tl}B_z)_i - (^{Tl}P_z)_i)^2$$

$$^{Tl}S_i = \frac{((^{Tl}B_x)_i - (^{Tl}P_x)_i, (^{Tl}B_y)_i - (^{Tl}P_y)_i, (^{Tl}B_z)_i - (^{Tl}P_z)_i)}{l_i} \quad i=1 \text{ to } 6$$

$$^{Tl}S_{0i} = ^{Tl}B_i \times ^{Tl}S_i$$

The Jacobian for the given pose is

$$^{Tl}J = ^{Tl} \begin{bmatrix} S_1 & S_2 & S_3 & S_4 & S_5 & S_6 \\ S_{01} & S_{02} & S_{03} & S_{04} & S_{05} & S_{06} \end{bmatrix}$$

C.1.2 Calculating Strut and Tooltip Displacements

The Jacobian may be used to calculate the effect of small changes in tooltip position relative to the tool tip ($d\mathbf{X}$) on the strut length ($d\mathbf{L}$) given a nominal mechanism pose.

$$\begin{aligned}d\mathbf{L} &= {}^{Tl}J^T d\mathbf{X} \\d\mathbf{L} &= (dl_1, dl_2, dl_3, dl_4, dl_5, dl_6)^T \\d\mathbf{X} &= (dx, dy, dz, d\theta_x, d\theta_y, d\theta_z)^T\end{aligned}$$

By inverting J , the effect of small strut length changes on the displacement at the tooltip relative to the tool tip may be calculated:

$$d\mathbf{X} = {}^{Tl}J^{-T} d\mathbf{L}$$

C.1.3 Calculating Axial Strut Forces

Given a 6x1 vector of the axial forces (\mathbf{f}) acting along the strut lines of action, the wrench (\mathbf{w}) acting at the tool tip on the platform is

$$\begin{aligned}\hat{\mathbf{w}} &= {}^{Tl}J\mathbf{f} \\ \hat{\mathbf{w}} &= (F_x, F_y, F_z, M_x, M_y, M_z)^T \\ \mathbf{f} &= (f_1, f_2, f_3, f_4, f_5, f_6)^T\end{aligned}$$

A gravitational load on the platform would be represented as $\mathbf{M}_w = (0, 0, -mg, 0, 0, 0)$.

By inverting J , the axial strut forces may be calculated given the wrench applied to the platform:

$$\mathbf{f} = {}^{Tl}J^{-1} \hat{\mathbf{w}}$$

C.1.4 Axial Strut Displacement from Externally Applied Forces

Assuming all of the struts are two-force members, the effects of friction in the base and platform joints are negligible, the modulus of elasticity and cross-sectional area for all of the struts is the same, the stiffness matrix K is

$$K = EA \begin{bmatrix} 1/l_1 & 0 & 0 & 0 & 0 & 0 \\ 0 & 1/l_2 & 0 & 0 & 0 & 0 \\ 0 & 0 & 1/l_3 & 0 & 0 & 0 \\ 0 & 0 & 0 & 1/l_4 & 0 & 0 \\ 0 & 0 & 0 & 0 & 1/l_5 & 0 \\ 0 & 0 & 0 & 0 & 0 & 1/l_6 \end{bmatrix}$$

Using the expressions for axial strut forces and small strut displacements, the amount of displacement in the struts caused by an externally applied load on the flexible structure may be calculated:

$$\begin{aligned} d\hat{X} &= (JKJ^T)^{-1} \hat{w} \\ d\hat{L} &= J^T d\hat{X} \end{aligned}$$

C.2 Tool Path Planning with Single Fixed-Length Strut

The objective is to create a motion program which will move the spindle nose in space while holding a particular strut at an arbitrary fixed length. In doing so, the platform joint of the chosen strut will traverse a path on the surface of a sphere with its center at the base joint of the chosen strut.

The desired strut “ i ” (with nominal base joint center location ${}^M B_i$), and the desired fixed length l_i are selected. The path which the platform joint ${}^M P_i$ is to follow is chosen.

The path is dependent upon the mobility constraints of the particular machine (strut extension and spherical joint limits, obstructions in the workvolume such as tool changers, etc.). Since the platform and the strut will have gage points attached to them which will be measured at particular instants during the motion program, the path is also dependent upon the workspace of the particular measuring instrument used. No matter how the path is constructed, every point ${}^M P_{ij}$ on the path must satisfy the equation of the sphere to guarantee that the strut length remains constant at each point on the path.

$$l_i^2 = ({}^M P_x)_{i,j} - ({}^M B_x)_i)^2 + ({}^M P_y)_{i,j} - ({}^M B_y)_i)^2 + ({}^M P_z)_{i,j} - ({}^M B_z)_i)^2$$

Once the platform joint path is chosen, the corresponding spindle nose position for each path point must be calculated. The first step in this process is to select the orientation of the platform about the (x,y,z) axes of the M system at each point on the path. The orientation may be constant for all points, or may be allowed to vary from point to point. In any case, the orientation ${}^M(\alpha, \beta, \gamma)_j$ for the j^{th} path point has the rotation matrix:

$$({}^M R_P)_j = \begin{bmatrix} \cos \beta \cos \gamma + \sin \alpha \sin \beta \sin \gamma & -\cos \beta \sin \gamma + \sin \alpha \sin \beta \cos \gamma & \cos \alpha \sin \beta \\ \cos \alpha \sin \gamma & \cos \alpha \cos \gamma & -\sin \alpha \\ -\sin \beta \cos \gamma + \sin \alpha \cos \beta \sin \gamma & \sin \beta \sin \gamma + \sin \alpha \cos \beta \cos \gamma & \cos \alpha \cos \beta \end{bmatrix}$$

Knowing the nominal position of the spindle nose position relative to the chosen platform joint center, the location of the spindle nose which will hold the strut at the nominal desired length is

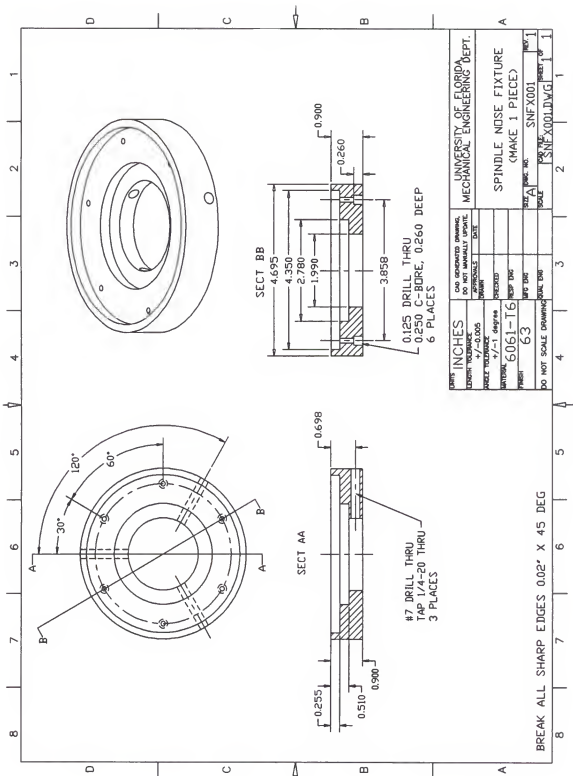
$$({}^M Tl)_{i,j} = ({}^M P)_{i,j} + ({}^M R_P)_j ({}^P Tl - ({}^P P)_i)$$

APPENDIX D

FIXTURE DESIGN DRAWINGS

This appendix contains the design drawings for:

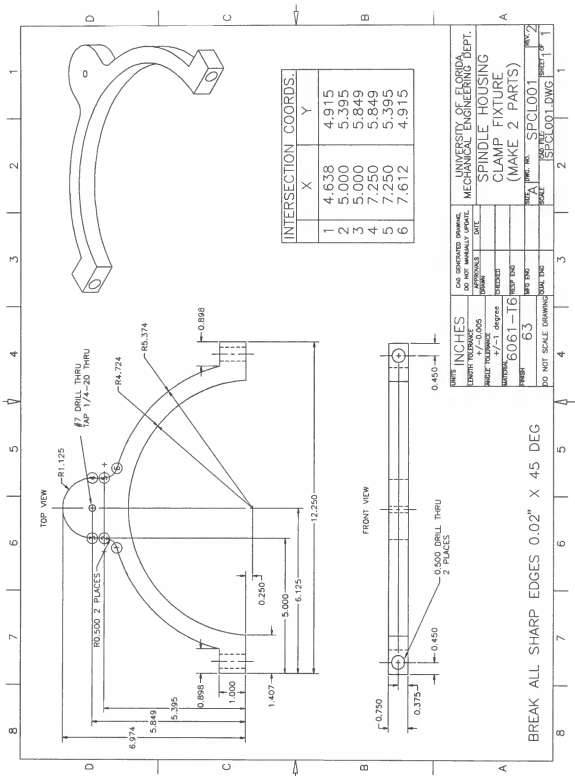
- 1 Gage point PR_2 - "Spindle Nose Fixture."
- 2 Gage point PR_2 - "Spindle Nose Ring Clamp."
- 3 Gage points PR_3 and PR_3 - "Spindle Housing Clamp Fixture."
- 4 Gage points SA and SB - "Leg Fixture Top."
- 5 Gage points SA and SB - "Leg Fixture Bottom."
- 6 Gage point SR - "Tool Holder Clamp Fixture."

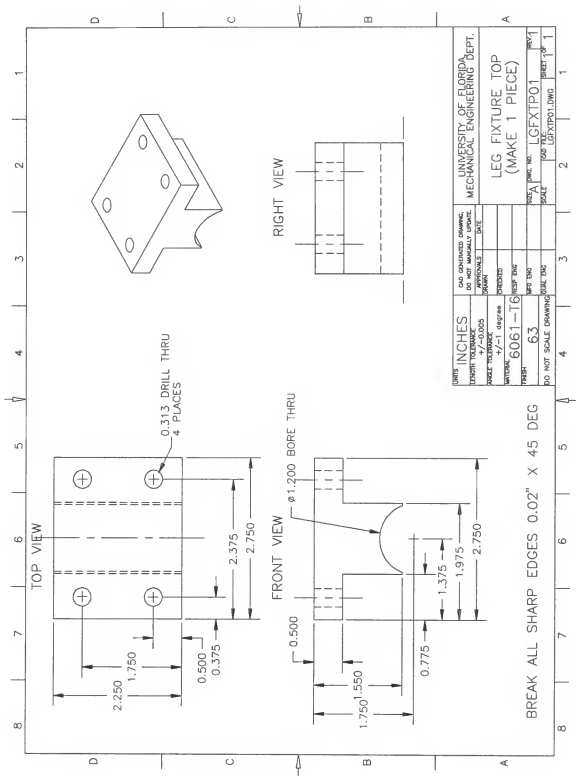


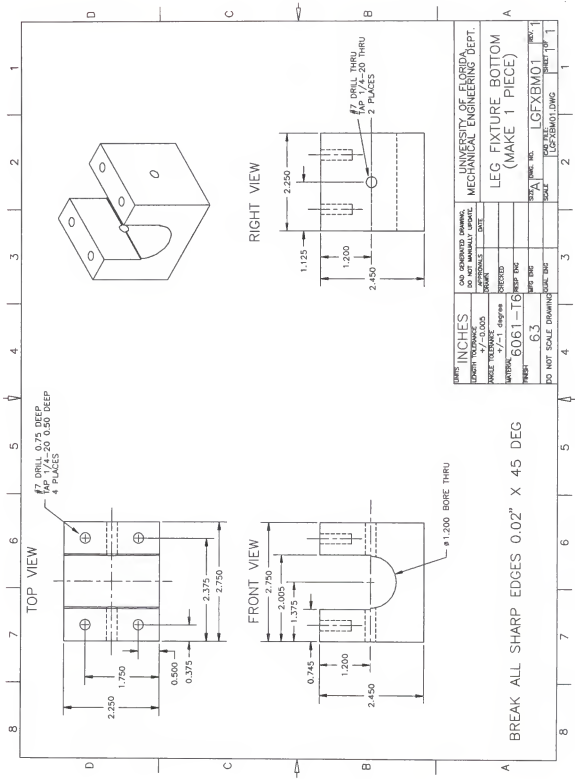
BREAK ALL SHARP EDGES 0.02" X 45 DEG

DATE	INCHES	NO. OF REVISED DRAWINGS	UNIVERSITY OF FLORIDA
	1/2" - 0.006	DO NOT REWALKLY UPDATE	MECHANICAL ENGINEERING DEPT.
SCALE	1/2" = 1" diameter	NO. OF WORKSHEET	
DATE	6061-16	YEAR MADE	SPINDLE NOSE RING CLAMP
PIECES	63	DATE TIME	(MAKE 1 PIECE)
DO NOT SCALE DRAWING		NO. OF WORKSHEET	SPINROO1
		NO. OF WORKSHEET	SPINROO1 DWG

	INTERSECTION	COORDS.
	X	Y
1	5.953	2.632
2	6.391	2.375
3	7.186	2.375
4	7.186	0.125
5	6.391	0.125
6	5.953	-0.132







#7 DRILL THRU
TAP 1/4"-20 1/2" DEEP 2 PLACES

#7 DRILL THRU $\sqrt{\phi 1.102^{+0.010}_{-0.000}}$ BORE THRU

FRONT VIEW

BREAK ALL SHARP EDGES 0.02" X45 DEG

[illegible]

BIBLIOGRAPHY

- 1 Shigley, J.E. and C.R. Mishke. Standard Handbook of Machine Design. New York: McGraw-Hill, 1986.
- 2 Moore, W. R. Foundations of Mechanical Accuracy. Bridgeport, Connecticut: The Moore Special Tool Company, 1970.
- 3 Slocum, A.M. Precision Machine Design. Englewood Cliffs, New Jersey: Prentice Hall 1992.
- 4 Kulkarni, R. "Design and Evaluation of a Technique to Find the Parametric Errors of a Numerically Controlled machine Tool Using a Laser Ball Bar." Masters Thesis, University of Florida 1996
- 5 Stewart, D. "A Platform with Six Degrees of Freedom." Proceedings of the Institution of Mechanical Engineers, Vol 180, Part 1, No. 15, 1966, pages 371-386.
- 6 Liu, K., John M. Fitzgerald and Frank L. Lewis. "Kinematic Analysis of a Stewart Platform Manipulator." IEEE Transactions on Industrial Electronics, Vol 40, No. 2, April 1993, pages 272-292.
- 7 Yang, H. and O. Masory. "Vibration Analysis of Stewart-Platforms." Boca Raton, Florida: Florida Atlantic University, Robotics Center.
- 8 Wang, Jian and Oren Masory. "On the Accuracy of a Stewart Platform - Part I The Effect of Manufacturing Tolerances." Proceedings IEEE International Conference on Robotics and Automation, Vol. 1, 1993. Los Alamitos, California: IEEE Computer Society Press, pages 114-120.
- 9 Masory, Oren, Jian Wang, and Hanqi Zhuang. "On the Accuracy of a Stewart Platform - Part II Kinematic Calibration and Compensation." Proceedings IEEE International Conference on Robotics and Automation, Vol. 1, 1993. Los Alamitos, California: IEEE Computer Society Press, pages 725-731.
- 10 Tajbakhsh, Hooman and Placid M. Ferreira. "Kinematic Error Estimation and Transmission Error Bounding for Stewart Platform Based Machine Tools." Transactions of NAMRI/SME, Vol 25, 1997. pages 323-328.

- 11 Zhuang, Hanqi and Zvi S. Roth. "Method for Kinematic Calibration of Stewart Platforms." Journal of Robotic Systems, Vol. 10, No. 3, 1993. pages 391-405
- 12 Zhuang, Hanqi. Lixin Liu and Oren Masory. "Autonomous Calibration of Hexapod Machine Tools." ASME Journal of Manufacturing Science and Technology, Vol 19, 1997. pages 202-211.
- 13 Bourdet, P., C. Lartigue, and F. Leveaux. "Effects of Data Point Distribution and Mathematical Model on Finding the Best-Fit Sphere to Data." Precision Engineering, Vol. 15 No. 3, 1993. pages 150-157.
- 14 Baldwin, Jon, Richard P. Henke, Kim D. Summerhays, Ronald M. Cassou, Curtis W. Brown. "Optimizing Discrete Point Sample Patterns and Measurement Data Analysis on Internal Cylindrical Surfaces with Systematic Form Deviations" Albuquerque: Sandia National Laboratories, SAND96 1996
- 15 Griffis, M., J. Duffy. "Kinesthetic Control: A Novel Theory for Simultaneously regulating Force and Displacement." Transactions of the ASME, Vol. 113 December 1991. pages 508-515
- 16 Alziade, R.I., Nazim R Tagiyev, J. Duffy. "A Forward and Reverse Displacement Analysis of an In-Parallel Spherical Manipulator." Mechanical Machine Theory, Vol. 29 No. 1, 1991 pages 125-137
- 17 Zhuang, Hanqi, Wen-Chiang Wu, Zvi S. Roth. "Camera assisted Calibration of SCARA Arms." Proceedings International Conference on Intelligent Robots and Systems, Vol. 1 1995. Los Alamitos, California: IEEE Computer Society Press, pages 507-512
- 18 Zhuang, Hanqi, Oren masory, Jiahua Yan. "Kinematic Calibration of a Stewart Platform Using Pose Measurements obtained by a Single Theodolite." Proceedings International Conference on Intelligent Robots and Systems, Vol. 2 1995. Los Alamitos, California: IEEE Computer Society Press, pages 329-334.
- 19 Sun, Chin-Huang Michael W. Griffis, Joseph Duffy. "Methodology for Comparing Stiffness Mappings Using Geometric Invariants." Robotics: Kinematics, Dynamics and Controls, ASME Vol. 72, 1994. pages 177-183.
- 20 Alziade, R.I., Nazim R Tagiyev, Joseph Duffy. "A Forward and Reverse Displacement Analysis of a 6-DOF In-Parallel Manipulator." Mechanical Machine Theory, Vol. 29 No. 1, 1994. pages 115-124
- 21 Griffis, M. and J. Duffy. "A Forward Displacement Analysis of a Class of Stewart Platforms." Journal of Robotic Systems, Vol. 6 No. 6, 1989. pages 703-720.

- 22 Baiges, Ivan J., Joseph Duffy. "Dynamic Modeling of Parallel Manipulators." Proceedings: ASME Design Engineering Technical Conferences and Computers in Engineering Conference, ASME 1996. pages 1-7
- 23 Griffis, M., J. Duffy. "On a General Model of Spatial Stiffness" Proceedings: CISM Symposium on Theory and Practice of Robots and Manipulators, Cracow, Poland. CISM 1990. pages 40-47.
- 24 Pang, Hysunok, Moshen Shahinpoor. "Analysis of Static Equilibrium of a Parallel Manipulator." Robotica, Vol. 11, 1993. pages 433-443.
- 25 Prischow, G., K.H. Wurst. "LINAPOD - Ein Baukastensystem fur Stabkinematikmaschinen." Werkstattstechnik, Vol. 87, 1997. pages 437-440.
- 26 Martinez, Jose M.R., Joseph Duffy. "An Application of Screw Algebra to the Acceleration Analysis of Serial Chains." Mechanical Machine Theory, Vol. 31, No. 4, 1996. pages 445-457.
- 27 Taylor, Barry N., Chris E. Kuyatt. "Guidelines for Evaluating and Expressing the Uncertainty of NIST Measurement Results." National Institute of Standards and Technology, NIST Technical Note 1297, 1994.
- 28 Bryan, J. "International Status of Thermal Error Research" Annals of the CIRP, Vol. 39 No. 2 1990. pages 645-656.
- 29 Swyt, Dennis A. "Uncertainties in Dimensional Measurements Made at nonstandard Temperatures." Journal of Research of the National Institute of Standards and Technology, Vol. 99 No. 1, 1994. pages 31-44.
- 30 Estler, W. Tyler. "Accuracy Analysis of the Space Shuttle Solid Rocket Motor Profile Measuring Device." U.S. Department of Commerce National Institute of Standards and Technology, NISTIR 89-4171, 1989.
- 31 Jokiel, Bernhard. "Analysis of a Parallel Architecture Coordinate Measuring Machine." Masters Thesis, University of Florida 1996
- 32 Huang, Chin-Chou. "Self Calibration for a Hexapod Coordinate Measuring Machine." Ph.D. Dissertation, University of Florida, 1998.

BIOGRAPHICAL SKETCH

The author was born on May 28, 1971, just outside of Los Angeles in Saugus, California. During his early years, his family moved a great deal, flowing with the changing tides of the construction industry, in which his father Berni Jokiel, Sr., was a cost estimator and civil engineer. His mother Lois, claims that Bernhard's first word was "asphalt" (true story). Settling in Federal Way, Washington, and moving later to Issaquah, Washington, he grew up attending public school excelling in math, science and music. At about five years of age, his parents bought him his first Lego building set, which fast became his favorite toy. As the years rolled on, it became apparent that his interests in math, science and computers were shaping him up to be an engineer.

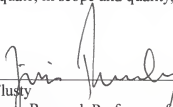
Graduating in 1989 from Liberty High School in Issaquah, he enrolled in mechanical engineering at the Florida Institute of Technology in Melbourne, Florida. Graduating in a grim job market in 1993, he considered himself lucky to find a third-shift job at a machine shop in town, and found a new interest in manufacturing and programming CNC milling machines. In 1994, he received a NSF Fellowship to the University of Florida Machine Tool Research Center. After completing his master's degree in 1996, he took a year-long internship at Sandia National Laboratories in California. He returned to UF in 1997 to pursue his Ph.D. In 1999 he starts a new career with Sandia National Laboratories Applied Manufacturing Processes Laboratory.

I certify that I have read this study and that in my opinion it conforms to acceptable standards of scholarly presentation and is fully adequate, in scope and quality, as a dissertation for the degree of Doctor of Philosophy.



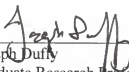
John C. Ziegert, Chairman
Associate Professor of
Mechanical Engineering

I certify that I have read this study and that in my opinion it conforms to acceptable standards of scholarly presentation and is fully adequate, in scope and quality, as a dissertation for the degree of Doctor of Philosophy.



Jiri Tlustý
Graduate Research Professor of
Mechanical Engineering

I certify that I have read this study and that in my opinion it conforms to acceptable standards of scholarly presentation and is fully adequate, in scope and quality, as a dissertation for the degree of Doctor of Philosophy.



Joseph Duffy
Graduate Research Professor of
Mechanical Engineering

I certify that I have read this study and that in my opinion it conforms to acceptable standards of scholarly presentation and is fully adequate, in scope and quality, as a dissertation for the degree of Doctor of Philosophy.



Gloria Wiens
Associate Professor of
Mechanical Engineering


I certify that I have read this study and that in my opinion it conforms to acceptable standards of scholarly presentation and is fully adequate, in scope and quality, as a dissertation for the degree of Doctor of Philosophy.



Suleyman Tufekci
Associate Professor of Industrial
and Systems Engineering

This dissertation was submitted to the Graduate Faculty of the College of Engineering and to the Graduate School and was accepted as partial fulfillment of the requirements for the degree of Doctor of Philosophy.

August 1999



M. J. Ohanian
Dean, College of Engineering



Winfred M. Phillips
Dean, Graduate School